DiffusionCLIP: Text-Guided Diffusion Models for Robust Image Manipulation

Gwanghyun Kim[1]   Taesung Kwon[1]   Jong Chul Ye[2,1]

Dept. of Bio and Brain Engineering[1], Kim Jaechul Graduate School of AI[2]

Korea Advanced Institute of Science and Technology (KAIST), Daejeon, Korea

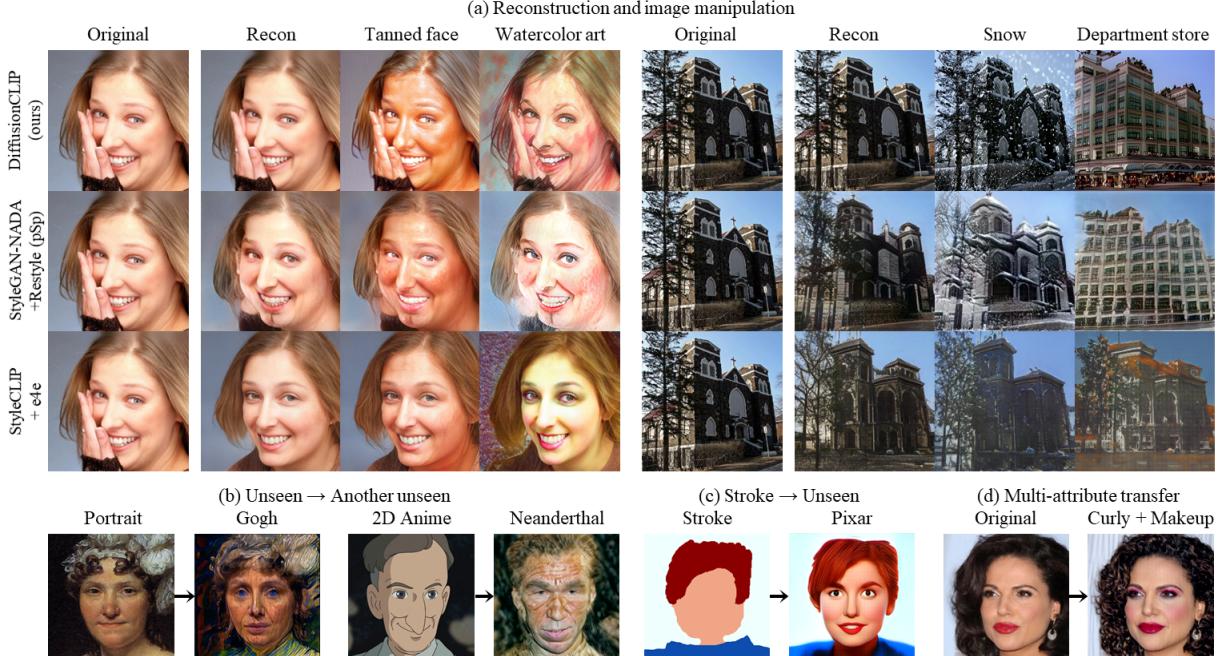{gwang.kim, star.kwon, jong.ye}@kaist.ac.kr

Figure 1. DiffusionCLIP enables faithful text-driven manipulation of real images by (a) preserving important details when the state-of-the-art GAN inversion-based methods fail. Other novel applications include (b) image translation between two unseen domains, (c) stroke-conditioned image synthesis to an unseen domain, and (d) multi-attribute transfer.

Abstract

Recently, GAN inversion methods combined with Contrastive Language-Image Pretraining (CLIP) enables zero-shot image manipulation guided by text prompts. However, their applications to diverse real images are still difficult due to the limited GAN inversion capability. Specifically, these approaches often have difficulties in reconstructing images with novel poses, views, and highly variable contents compared to the training data, altering object identity, or producing unwanted image artifacts. To mitigate these problems and enable faithful manipulation of real images, we propose a novel method, dubbed DiffusionCLIP, that performs text-driven image manipulation using diffusion models. Based on full inversion capability and high-quality image generation power of recent diffusion models, our method performs zero-shot image manipulation successfully even between unseen domains and takes another step towards general application by manipulating images from a widely varying ImageNet dataset. Furthermore, we propose a novel noise combination method that allows straightforward multi-attribute manipulation. Extensive experiments and human evaluation confirmed robust and superior manipulation performance of our methods compared to the existing baselines. Code is available at https://github.com/gwang-kim/DiffusionCLIP.git

1. Introduction

Recently, GAN inversion methods [1–4, 7, 45, 55] combined with Contrastive Language-Image Pretraining (CLIP)

[41] has become popular thanks to their ability for zero-shot image manipulation guided by text prompts [20, 39]. Nevertheless, its real-world application on diverse types of images is still tricky due to the limited GAN inversion performance.

Specifically, successful manipulation of images should convert the image attribute to that of the target without unintended changes of the input content. Unfortunately, the current state-of-the-art (SOTA) encoder-based GAN inversion approaches [3, 45, 55] often fail to reconstruct images with novel poses, views, and details. For example, in the left panel of Fig. 1(a), e4e [55] and ReStyle [3] with pSp encoder [45] fail to reconstruct unexpected hand on the cheek, inducing the unintended change. This is because they have rarely seen such faces with hands during the training phase. This issue becomes even worse in the case of images from a dataset with high variance such as church images in LSUN-Church [64] and ImageNet [49] dataset. As shown in the right panel of Fig. 1(a) for the conversion to a department store, existing GAN inversion methods produce artificial architectures that can be perceived as different buildings.

Recently, diffusion models such as denoising diffusion probabilistic models (DDPM) [23, 51] and score-based generative models [53, 54] have achieved great successes in image generation tasks [23, 26, 52, 54]. The latest works [16, 54] have demonstrated even higher quality of image synthesis performance compared to variational autoencoders (VAEs) [31, 37, 43], flows [17, 30, 44], auto-regressive models [34, 56], and generative adversarial networks (GANs) [6, 21, 28, 29]. Furthermore, a recent denoising diffusion implicit models (DDIM) [52] further accelerates sampling procedure and enables nearly perfect inversion [16].

Inspired by this, here we propose a novel DiffusionCLIP - a CLIP-guided robust image manipulation method by diffusion models. Here, an input image is first converted to the latent noises through a forward diffusion. In the case of DDIM, the latent noises can be then inverted nearly perfectly to the original image using a reverse diffusion if the score function for the reverse diffusion is retained the same as that of the forward diffusion. Therefore, the key idea of DiffusionCLIP is to fine-tune the score function in the reverse diffusion process using a CLIP loss that controls the attributes of the generated image based on the text prompts.

Accordingly, DiffusionCLIP can successfully perform image manipulation both in the trained and unseen domain (Fig. 1(a)). We can even translate the image from an unseen domain into another unseen domain (Fig. 1(b)), or generate images in an unseen domain from the strokes (Fig. 1(c)). Moreover, by simply combining the noise predicted from several fine-tuned models, multiple attributes can be changed simultaneously through only one sampling process (Fig. 1(d)). Furthermore, DiffsuionCLIP takes another step towards general application by manipulating images from a widely varying ImageNet [49] dataset (Fig. 6), which has been rarely

explored with GAN-inversion due to its inferior reconstruction. [5, 13]

Additionally, we propose a systematic approach to find the optimal sampling conditions that lead to high quality and speedy image manipulation. Qualitative comparison and human evaluation results demonstrate that our method can provide robust and accurate image manipulation, outperforming SOTA baselines.

2. Related Works

2.1. Diffusion Models

Diffusion probabilistic models [23, 51] are a type of latent variable models that consist of a forward diffusion process and a reverse diffusion process. The forward process is a Markov chain where noise is gradually added to the data when sequentially sampling the latent variables $\boldsymbol{x}_t$ for $t = 1, \cdots, T$. Each step in the forward process is a Gaussian transition $q(\boldsymbol{x}_t \mid \boldsymbol{x}_{t-1}) := \mathcal{N}(\sqrt{1-\beta_t}\boldsymbol{x}_{t-1}, \beta_t\mathbf{I})$, where $\{\beta_t\}_{t=0}^{T}$ are fixed or learned variance schedule. The resulting latent variable $\boldsymbol{x}_t$ can be expressed as:

$$\boldsymbol{x}_t = \sqrt{\alpha_t}\boldsymbol{x}_0 + \sqrt{1-\alpha_t}\boldsymbol{w}, \quad \boldsymbol{w} \sim \mathcal{N}(\mathbf{0}, \mathbf{I}), \quad (1)$$

where $\alpha_t := \prod_{s=1}^{t}(1-\beta_s)$. The reverse process $q(\boldsymbol{x}_{t-1} \mid \boldsymbol{x}_t)$ is parametrized by another Gaussian transition $p_\theta(\boldsymbol{x}_{t-1} \mid \boldsymbol{x}_t) := \mathcal{N}(\boldsymbol{x}_{t-1}; \boldsymbol{\mu}_\theta(\boldsymbol{x}_t, t), \sigma_\theta(\boldsymbol{x}_t, t)\mathbf{I})$. $\boldsymbol{\mu}_\theta(\boldsymbol{x}_t, t)$ can be decomposed into the linear combination of $\boldsymbol{x}_t$ and a noise approximation model $\boldsymbol{\epsilon}_\theta(\boldsymbol{x}_t, t)$, which can be learned by solving the optimization problem as follows:

$$\min_\theta \mathbb{E}_{\boldsymbol{x}_0 \sim q(\boldsymbol{x}_0), \boldsymbol{w} \sim \mathcal{N}(\mathbf{0}, \mathbf{I}), t}||\boldsymbol{w} - \boldsymbol{\epsilon}_\theta(\boldsymbol{x}_t, t)||_2^2. \quad (2)$$

After training $\boldsymbol{\epsilon}_\theta(\boldsymbol{x}, t)$, the data is sampled using following reverse diffusion process:

$$\boldsymbol{x}_{t-1} = \frac{1}{\sqrt{1-\beta_t}}\left(\boldsymbol{x}_t - \frac{\beta_t}{\sqrt{1-\alpha_t}}\boldsymbol{\epsilon}_\theta(\boldsymbol{x}_t, t)\right) + \sigma_t\boldsymbol{z}, \quad (3)$$

where $\boldsymbol{z} \sim \mathcal{N}(\mathbf{0}, \mathbf{I})$. It was found that the sampling process of DDPM corresponds to that of the score-based generative models [53, 54] with the following relationship:

$$\boldsymbol{\epsilon}_\theta(\boldsymbol{x}_t, t) = -\sqrt{1-\alpha_t}\nabla_{\boldsymbol{x}_t}\log p_\theta(\boldsymbol{x}_t). \quad (4)$$

Meanwhile, [52] proposed an alternative non-Markovian noising process that has the same forward marginals as DDPM but has a distinct sampling process as follows:

$$\boldsymbol{x}_{t-1} = \sqrt{\alpha_{t-1}}\boldsymbol{f}_\theta(\boldsymbol{x}_t, t) + \sqrt{1-\alpha_{t-1}-\sigma_t^2}\boldsymbol{\epsilon}_\theta(\boldsymbol{x}_t, t) + \sigma_t^2\boldsymbol{z}, \quad (5)$$

where, $\boldsymbol{z} \sim \mathcal{N}(\mathbf{0}, \mathbf{I})$ and $\boldsymbol{f}_\theta(\boldsymbol{x}_t, t)$ is a the prediction of $\boldsymbol{x}_0$ at t given $\boldsymbol{x}_t$ and $\boldsymbol{\epsilon}_\theta(\boldsymbol{x}_t, t)$:

$$\boldsymbol{f}_\theta(\boldsymbol{x}_t, t) := \frac{\boldsymbol{x}_t - \sqrt{1-\alpha_t}\boldsymbol{\epsilon}_\theta(\boldsymbol{x}_t, t)}{\sqrt{\alpha_t}}. \quad (6)$$

This sampling allows using different samplers by changing the variance of the noise σ_t. Especially, by setting this noise to 0, which is a DDIM sampling process [52], the sampling process becomes deterministic, enabling full inversion of the latent variables into the original images with significantly fewer steps [16, 52]. In fact, DDIM can be considered as an Euler method to solve an ordinary differential equation (ODE) by rewriting Eq. 5 as follows:

$$\sqrt{\frac{1}{\alpha_{t-1}}}\boldsymbol{x}_{t-1} - \sqrt{\frac{1}{\alpha_t}}\boldsymbol{x}_t = \left(\sqrt{\frac{1}{\alpha_{t-1}} - 1} - \sqrt{\frac{1}{\alpha_t} - 1}\right)\boldsymbol{\epsilon}_\theta(\boldsymbol{x}_t, t). \tag{7}$$

For mathematical details, see Supplementary Section A.

2.2. CLIP Guidance for Image Manipulation

CLIP [41] was proposed to efficiently learn visual concepts with natural language supervision. In CLIP, a text encoder and an image encoder are pretrained to identify which texts are matched with which images in the dataset. Accordingly, we use a pretrained CLIP model for our text-driven image manipulation.

To effectively extract knowledge from CLIP, two different losses have been proposed: a global target loss [39], and local directional loss [20]. The global CLIP loss tries to minimize the cosine distance in the CLIP space between the generated image and a given target text as follows:

$$\mathcal{L}_{\text{global}}(\boldsymbol{x}_{\text{gen}}, y_{\text{tar}}) = D_{\text{CLIP}}(\boldsymbol{x}_{\text{gen}}, y_{\text{tar}}), \tag{8}$$

where y_{tar} is a text description of a target, $\boldsymbol{x}_{\text{gen}}$ denotes the generated image, and D_{CLIP} returns a cosine distance in the CLIP space between their encoded vectors. On the other hand, the local directional loss [20] is designed to alleviate the issues of global CLIP loss such as low diversity and susceptibility to adversarial attacks. The local directional CLIP loss induces the direction between the embeddings of the reference and generated images to be aligned with the direction between the embeddings of a pair of reference and target texts in the CLIP space as follows:

$$\mathcal{L}_{\text{direction}}\left(\boldsymbol{x}_{\text{gen}}, y_{\text{tar}}; \boldsymbol{x}_{\text{ref}}, y_{\text{ref}}\right) := 1 - \frac{\langle \Delta I, \Delta T \rangle}{\|\Delta I\|\|\Delta T\|}, \tag{9}$$

where

$$\Delta T = E_T(y_{\text{tar}}) - E_T(y_{\text{ref}}), \ \Delta I = E_I(\boldsymbol{x}_{\text{gen}}) - E_I(\boldsymbol{x}_{\text{ref}}).$$

Here, E_I and E_T are CLIP's image and text encoders, respectively, and $y_{\text{ref}}, \boldsymbol{x}_{\text{ref}}$ are the source domain text and image, respectively. The manipulated images guided by the directional CLIP loss are known robust to mode-collapse issues because by aligning the direction between the image representations with the direction between the reference text and the target text, distinct images should be generated. Also, it is more robust to adversarial attacks because the perturbation will be different depending on images [41]. More related works are illustrated in Supplementary Section A.

3. DiffusionCLIP

The overall flow of the proposed DiffusionCLIP for image manipulation is shown in Fig. 2. Here, the input image $\boldsymbol{x}_0$ is first converted to the latent $\boldsymbol{x}_{t_0}(\theta)$ using a pretrained diffusion model $\boldsymbol{\epsilon}_\theta$. Then, guided by the CLIP loss, the diffusion model at the reverse path is fine-tuned to generate samples driven by the target text y_{tar}. The deterministic forward-reverse processes are based on DDIM [52]. For translation between unseen domains, the latent generation is also done by forward DDPM [23] process as will be explained later.
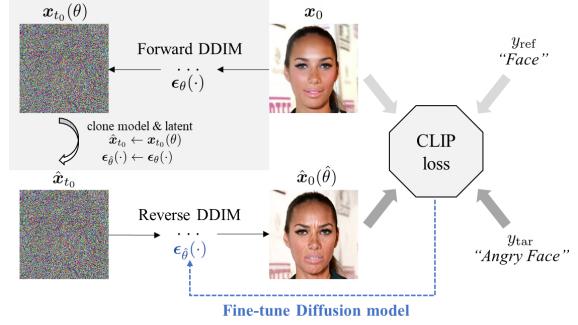

Figure 2. Overview of DiffusionCLIP. The input image is first converted to the latent via diffusion models. Then, guided by directional CLIP loss, the diffusion model is fine-tuned, and the updated sample is generated during reverse diffusion.

3.1. DiffusionCLIP Fine-tuning

In terms of fine-tuning, one could modify the latent or the diffusion model itself. We found that direct model fine-tuning is more effective, as analyzed in Supplementary Section D. Specifically, to fine-tune the reverse diffusion model $\boldsymbol{\epsilon}_\theta$, we use the following objective composed of the directional CLIP loss $\mathcal{L}_{\text{direction}}$ and the identity loss $\mathcal{L}_{\text{ID}}$:

$$\mathcal{L}_{\text{direction}}\left(\hat{\boldsymbol{x}}_0(\hat{\theta}), y_{\text{tar}}; \boldsymbol{x}_0, y_{\text{ref}}\right) + \mathcal{L}_{\text{id}}(\hat{\boldsymbol{x}}_0(\hat{\theta}), \boldsymbol{x}_0), \tag{10}$$

where $\boldsymbol{x}_0$ is the original image, $\hat{\boldsymbol{x}}_0(\hat{\theta})$ is the generated image from the latent $\boldsymbol{x}_{t_0}$ with the optimized parameter $\hat{\theta}$, y_{ref} is the reference text, y_{tar} is the target text given for image manipulation.

Here, the CLIP loss is the key component to supervise the optimization. Of two types of CLIP losses as discussed above, we employ directional CLIP loss as a guidance thanks to the appealing properties as mentioned in Section 2.2. For the text prompt, directional CLIP loss requires a reference text y_{ref} and a target text y_{tar} while training. For example, in the case of changing the expression of a given face image into an angry expression, we can use 'face' as a reference text and 'angry face' as a target text. In this paper, we often use concise words to refer to each text prompt (e.g. 'tanned face' to 'tanned').

The identity loss $\mathcal{L}_{\text{id}}$ is employed to prevent the unwanted changes and preserve the identity of the object. We generally use ℓ_1 loss as identity loss, and in case of human face image manipulation, face identity loss in [15] is added:

$$\mathcal{L}_{\text{id}}(\hat{\boldsymbol{x}}_0(\hat{\theta}), \boldsymbol{x}_0) = \lambda_{\text{L1}}\|\boldsymbol{x}_0 - \hat{\boldsymbol{x}}_0(\hat{\theta})\| + \lambda_{\text{face}}\mathcal{L}_{\text{face}}(\hat{\boldsymbol{x}}_0(\hat{\theta}), \boldsymbol{x}_0),$$
(11)

where $\mathcal{L}_{\text{face}}$ is the face identity loss [15], and $\lambda_{\text{L1}} \geq 0$ and $\lambda_{\text{face}} \geq 0$ are weight parameters for each loss. The necessity of identity losses depends on the types of the control. For some controls, the preservation of pixel similarity and the human identity are significant (e.g. expression, hair color) while others prefer the severe shape and color changes (e.g. artworks, change of species).
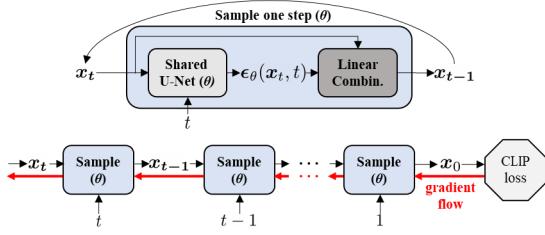

Figure 3. Gradient flows during fine-tuning the diffusion model with the shared architecture across t.

Existing diffusion models [16, 23, 52] adopt the shared U-Net [47] architecture for all t, by inserting the information of t using sinusoidal position embedding as used in the Transformer [57]. With this architecture, the gradient flow during DiffusionCLIP fine-tuning can be represented as Fig. 3, which is a similar process of training recursive neural network [48].

Once the diffusion model is fine-tuned, any image from the pretrained domain can be manipulated into the image corresponding to the target text y_{tar} as illustrated in Fig. 4(a). For details of the fine-tuning procedure and the model architecture, see Supplementary Section B and C.

3.2. Forward Diffusion and Generative Process

As the DDPM sampling process in Eq. 3 is stochastic, the samples generated from the same latent will be different every time. Even if the sampling process is deterministic, the forward process of DDPM, where the random Gaussian noise is added as in Eq. 1, is also stochastic, hence the reconstruction of the original image is not guaranteed. To fully leverage the image synthesis performance of diffusion models with the purpose of image manipulation, we require the deterministic process both in the forward and reverse direction with pretrained diffusion models for successful image manipulation. On the other hand, for the image translation between unseen domains, stochastic sampling by DDPM is often helpful, which will be discussed in more detail later.

For the full inversion, we adopt deterministic reverse DDIM process [16, 52] as generative process and ODE ap-

proximation of its reversal as a forward diffusion process. Specifically, the deterministic forward DDIM process to obtain latent is represented as:

$$\boldsymbol{x}_{t+1} = \sqrt{\alpha_{t+1}}\boldsymbol{f}_\theta(\boldsymbol{x}_t, t) + \sqrt{1 - \alpha_{t+1}}\boldsymbol{\epsilon}_\theta(\boldsymbol{x}_t, t) \quad (12)$$

and the deterministic reverse DDIM process to generate sample from the obtained latent becomes:

$$\boldsymbol{x}_{t-1} = \sqrt{\alpha_{t-1}}\boldsymbol{f}_\theta(\boldsymbol{x}_t, t) + \sqrt{1 - \alpha_{t-1}}\boldsymbol{\epsilon}_\theta(\boldsymbol{x}_t, t) \quad (13)$$

where $\boldsymbol{f}_\theta$ is defined in Eq. 24. For the derivations of ODE approximation, see Supplementary Sec A.

Another important contribution of DiffusionCLIP is a fast sampling strategy. Specifically, instead of performing forward diffusion until the last time step T, we found that we can accelerate the forward diffusion by performing up to $t_0 < T$, which we call 'return step'. We can further accelerate training by using fewer discretization steps between $[1, t_0]$, denoted as S_{for} and S_{gen} for forward diffusion and generative process, respectively [52]. Through qualitative and quantitative analyses, we found the optimal groups of hyperparameters for t_0, S_{for} and S_{gen}. For example, when T is set to 1000 as a common choice [16, 23, 52], the choices of $t_0 \in [300, 600]$ and $(S_{\text{for}}, S_{\text{gen}}) = (40, 6)$ satisfy our goal. Although $S_{\text{gen}} = 6$ may give imperfect reconstruction, we found that the identity of the object that is required for training is preserved sufficiently. We will show the results of quantitative and qualitative analyses on $S_{\text{for}}, S_{\text{gen}}$ and t_0 later through experiments and Supplementary Section F.

Lastly, if several latents have been precomputed (grey square region in Fig. 2), we can further reduce the time for fine-tuning by recycling the latent to synthesize other attributes. With these settings, the fine-tuning is finished in 1~7 minutes on NVIDIA Quardro RTX 6000.

3.3. Image Translation between Unseen Domains

The fine-tuned models through DiffusionCLIP can be leveraged to perform the additional novel image manipulation tasks as shown in Fig. 4.

First, we can perform image translation from an unseen domain to another unseen domain, and stroke-conditioned image synthesis in an unseen domain as described in Fig. 4(b) and (c), respectively. A key idea to address this difficult problem is to bridge between two domains by inserting the diffusion models trained on the dataset that is relatively easy to collect. Specifically, in [9, 33], it was found that with pretrained diffusion models, images trained from the unseen domain can be translated into the images in the trained domain. By combining this method with DiffsuionCLIP, we can now translate the images in zero-shot settings for both source and target domains. Specifically, the images in the source unseen domain $\boldsymbol{x}_0$ are first perturbed through the forward DDPM process in Eq. 1 until enough time step t_0 when
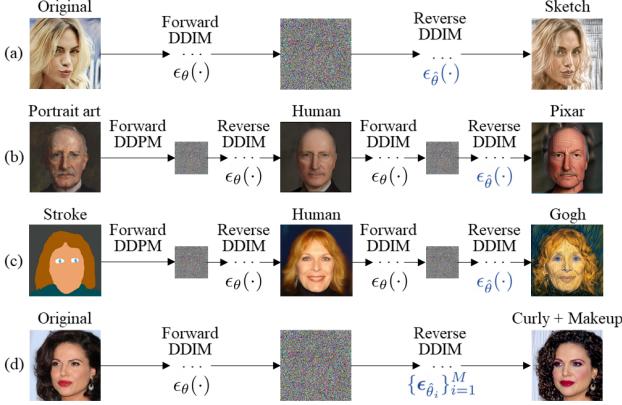
Figure 4. Novel applications of DiffusionCLIP. (a) Manipulation of images in pretrained domain to CLIP-guided domain. (b) Image translation between unseen domains. (c) Stroke-conditioned image generation in an unseen domain. (d) Multi-attribute transfer. ϵ_θ and $\epsilon_{\hat{\theta}}$ indicate the original pretrained and fine-tuned diffusion models, respectively.

the domain-related component are blurred but the identity or semantics of object is preserved. This is usually set to 500. Next, the images in the pretrained domain x'_0 are sampled with the original pretrained model ϵ_θ using reverse DDIM process in Eq. 13. Then, x'_0 is manipulated into the image $\hat{x}_0$ in the CLIP-guided unseen domain as we do in Fig. 4(a) with the fine-tuned model $\epsilon_{\hat{\theta}}$.

3.4. Noise Combination

Multi-attribute transfer. We discover that when the noises predicted from multiple fine-tuned models $\{\epsilon_{\hat{\theta}_i}\}_{i=1}^M$ are combined during the sampling, multiple attributes can be changed through only one sampling process as described in Fig. 4(d). Therefore, we can flexibly mix several single attribute fine-tuned models with different combinations without having to fine-tune new models with target texts that define multiple attributes. In detail, we first invert the image with the original pretrained diffusion model and use the multiple diffusion models by the following sampling rule:

$$
\begin{aligned}
x_{t-1} = &\sqrt{\alpha_{t-1}} \sum_{i=1}^M \gamma_i(t) f_{\hat{\theta}_i}(x_t, t) \\
&+ \sqrt{1 - \alpha_{t-1}} \sum_{i=1}^M \gamma_i(t) \epsilon_{\hat{\theta}_i}(x_t, t),
\end{aligned}
\tag{14}
$$

where $\{\gamma_i(t)\}_{t=1}^T$ is the sequence of weights of each fine-tuned model $\epsilon_{\hat{\theta}_i}$ satisfying $\sum_{i=1}^M \gamma_i(t) = 1$, which can be used for controlling the degree of each attribute. From Eq. 4, we can interpret this sampling process as increasing the joint probability of conditional distributions as following:

$$
\sum_{i=1}^M \gamma_i(t) \epsilon_{\hat{\theta}_i}(x_t, t) \propto -\nabla_{x_t} \log \prod_{i=1}^M p_{\hat{\theta}_i}(x_t | y_{tar,i})^{\gamma_i(t)},
\tag{15}
$$

where $y_{tar, i}$ is the target text for each fine-tuned model $\epsilon_{\hat{\theta}_i}$.

In the existing works [10, 11], users require the combination of tricky task-specific loss designs or dataset preparation

with large manual effort for the task, while ours enable the task in a natural way without such effort.

Continuous transition. We can also apply the above noise combination method for controlling the degree of change during single attribute manipulation. By mixing the noise from the original pretrained model ϵ_θ and the fine-tuned model $\epsilon_{\hat{\theta}}$ with respect to a degree of change $\gamma \in [0, 1]$, we can perform interpolation between the original image and the manipulated image smoothly.

For more details and pseudo-codes of the aforementioned applications, see Supplementary Section B.

4. Experiments

For all manipulation results by DiffusionCLIP, we use 256^2 size of images. We used the models pretrained on CelebA-HQ [27], AFHQ-Dog [12], LSUN-Bedroom and LSUN-Church [64] datasets for manipulating images of human faces, dogs, bedrooms, and churches, respectively. We use images from the testset of these datasets for the test. To fine-tune diffusion models, we use Adam optmizer with an initial learning rate of 4e-6 which is increased linearly by 1.2 per 50 iterations. We set λ_{L1} and λ_{ID} to 0.3 and 0.3 if used. As mentioned in Section 3.2, we set t_0 in [300, 600] when the total timestep T is 1000. We set $(S_{for}, S_{gen}) = (40, 6)$ for training; and to $(200, 40)$ for the test time. Also, we precomputed the latents of 50 real images of size 256^2 in each training set of pretrained dataset. For more detailed hyperparameter settings, see Supplementary Section F.

Table 1. Quantitative comparison for face image reconstruction.

Method	MAE ↓	LPIPS ↓	SSIM ↑
Optimization	0.061	0.126	0.875
pSp	0.079	0.169	0.793
e4e	0.092	0.221	0.742
ReStyle w pSp	0.073	0.145	0.823
ReStyle w e4e	0.089	0.202	0.758
HFGI w e4e	0.062	0.127	0.877
Diffusion ($t_0 = 300$)	**0.020**	**0.073**	**0.914**
Diffusion ($t_0 = 400$)	0.021	0.076	0.910
Diffusion ($t_0 = 500$)	0.022	0.082	0.901
Diffusion ($t_0 = 600$)	0.024	0.087	0.893

Table 2. Human evaluation results of real image manipulation on CelebA-HQ [27]. The reported values mean the preference rate of results from DiffusionCLIP against each method.

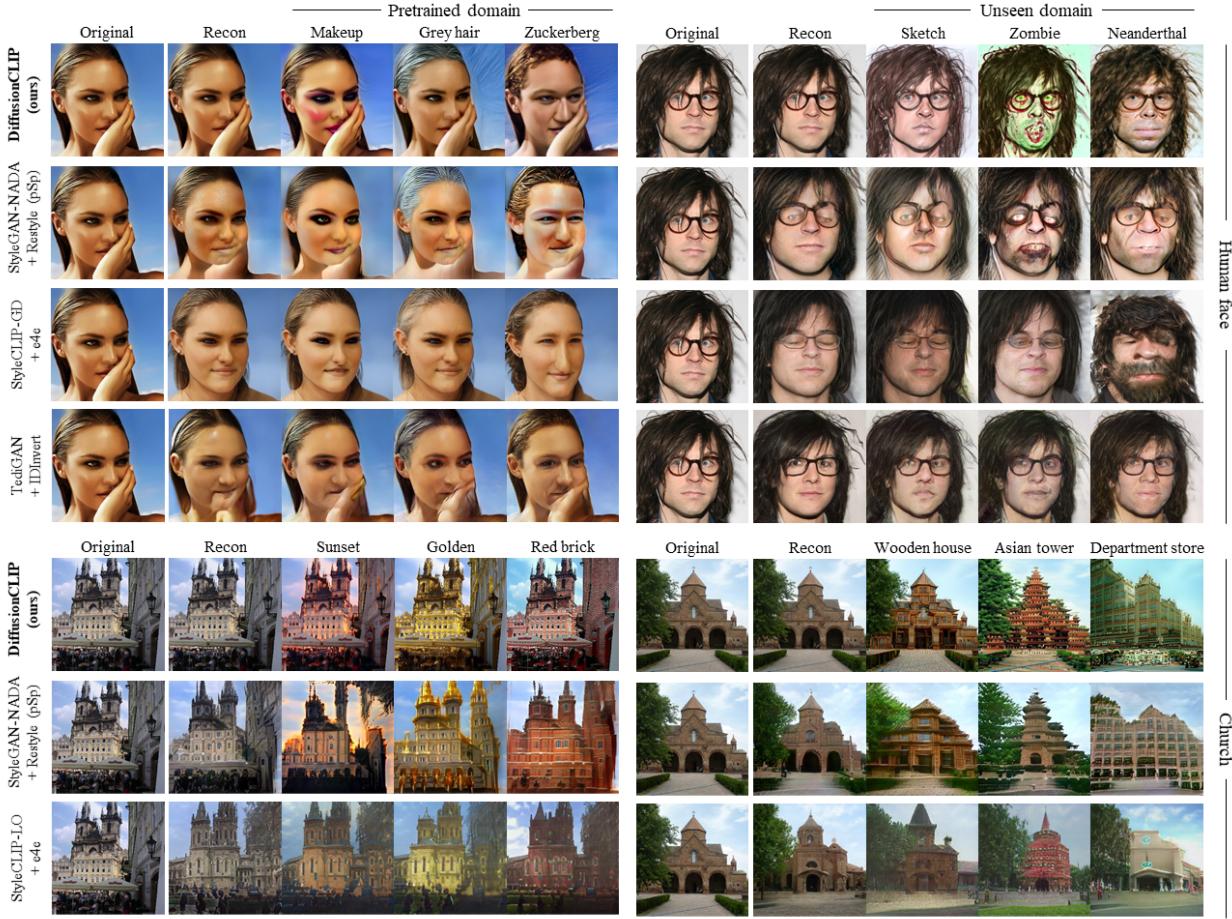| vs		StyleGAN-NADA (+ Restyle w pSp)	StyleCLIP (+ e4e)
Hard cases	In-domain	69.85%	69.65%
	Out-of-domain	79.60%	94.60%
	All domains	73.10%	77.97%
General cases	In-domain	58.05%	50.10%
	Out-of-domain	71.03%	88.90%
	All domains	62.47%	63.03%

Figure 5. Comparison with the state-of-the-art text-driven manipulation methods: TediGAN [62], StyleCLIP [39] and StyleGAN-NADA [20]. StyleCLIP-LO and StyleCLIP-GD refer to the latent optimization (LO) and global direction (GD) methods of StyleCLIP.
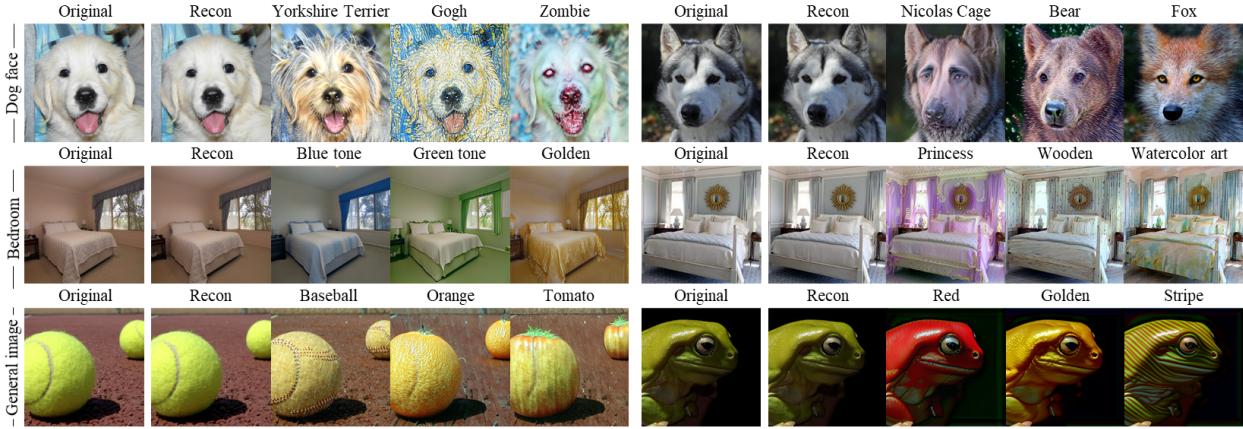

Figure 6. Manipulation results of real dog face, bedroom and general images using DiffusionCLIP.

4.1. Comparison and Evaluation

Reconstruction. To demonstrate the nearly perfect reconstruction performance of our method, we perform the quantitative comparison with SOTA GAN inversion methods, pSp [45], e4e [55], ReStyle [3] and HFGI [58]. As in Tab. 1, our method shows higher reconstruction quality than all baselines in terms of all metrics: MAE, SSIM and LPIPS [66].

Qualitative comparison. For the qualitative comparison of manipulation performance with other methods, we use the state-of-the-art text manipulation methods, TediGAN [62], StyleCLIP [39] and StyleGAN-NADA [20] where images

6

Table 3. Quantitative evaluation results. Our goal is to achieve the better score in terms of Directional CLIP similarity ($\mathcal{S}_{\mathrm{dir}}$), segmentation-consistency (SC), and face identity similarity (ID).

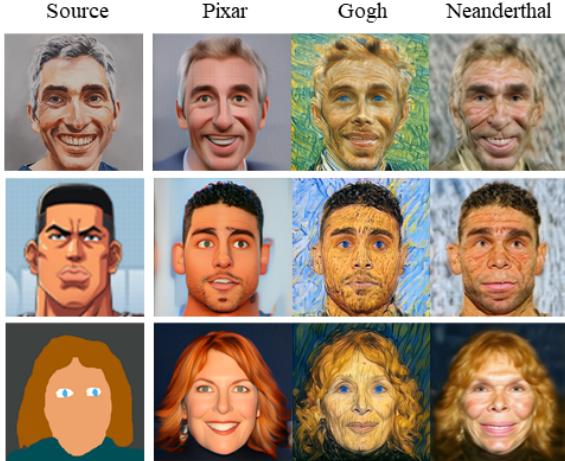|	CelebA-HQ			LSUN-Church	
	$\mathcal{S}_{\mathrm{dir}}\uparrow$	SC$\uparrow$	ID$\uparrow$	$\mathcal{S}_{\mathrm{dir}}\uparrow$	SC$\uparrow$
StyleCLIP	0.13	86.8%	0.35	0.13	67.9%
StyleGAN-NADA	0.16	89.4%	0.42	0.15	73.2%
DiffusionCLIP (Ours)	**0.17**	**93.7%**	**0.70**	**0.20**	**78.1%**

Figure 7. Results of image translation between unseen domains.

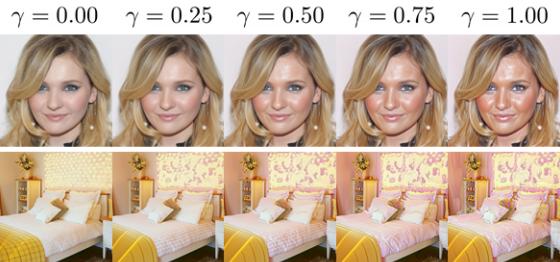Figure 8. Results of multi-attribute transfer.

Figure 9. Results of continuous transition.

for the target control is not required similar to our method. StyleGAN2 [29] pretrained on FFHQ-1024 [28] and LSUN-Church-256 [64] is used for StyleCLIP and StyleGAN-NADA. StyleGAN [28] pretrained on FFHQ-256 [28] is used for TediGAN. For GAN inversion, e4e encoder [55] is used for StyleCLIP latent optimization (LO) and global
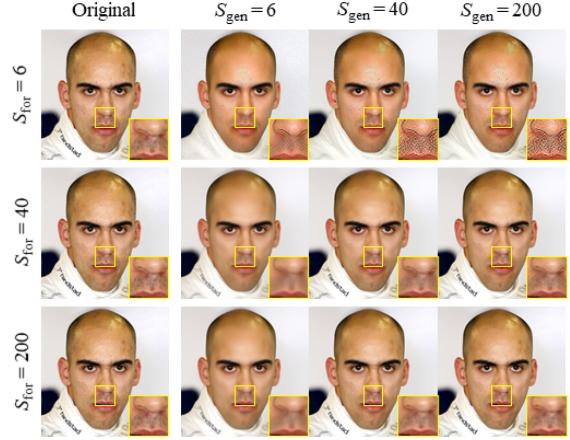

Figure 10. Reconstruction results varying the number of forward diffusion steps S_{for} and generative steps S_{gen}.
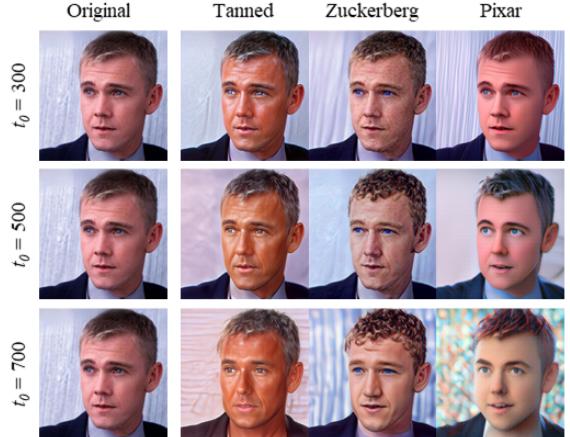

Figure 11. Manipulation results depending on t_0 values.

direction (GD), Restyle encoder [3] with pSp [45] is used for StyleGAN-NADA, and IDInvert [69] is used for Tedi-GAN, as in their original papers. Face alignment algorithm is used for StyleCLIP and StyleGAN-NADA as their official implementations. Our method uses DDPM pretrained on CelebA-HQ-256 [27] and LSUN-Church-256 [64].

As shown in Fig. 5, SOTA GAN inversion methods fail to manipulate face images with novel poses and details producing distorted results. Furthermore, in the case of church images, the manipulation results can be recognized as the results from different buildings. These results imply significant practical limitations. On the contrary, our reconstruction results are almost perfect even with fine details and background, which enables faithful manipulation. In addition to the manipulation in the pretrained domain, DiffusonCLIP can perform the manipulation into the unseen domain successfully, while StyleCLIP and TediGAN fail.

User study. We conduct user study to evaluate real face image manipulation performance on CelebA-HQ [27] with our method, StyleCLIP-GD [39] and StyleGAN-NADA [20].

We get 6000 votes from 50 people using a survey platform. We use the first 20 images in CelebA-HQ testset as general cases and use another 20 images with novel views, hand pose, and fine details as hard cases. For a fair comparison, we use 4 in-domain attributes (angry, makeup, beard, tanned) and 2 out-of-domain attributes (zombie, sketch), which are used in the studies of baselines. Here, we use official pre-trained checkpoints and implementation for each approach. As shown in Tab. 2, for both general cases and hard cases, all of the results from DiffusionCLIP are preferred compared to baselines ($> 50\%$). Of note, in hard cases, the preference rates for ours were all increased, demonstrating robust manipulation performance. It is remarkable that the high preference rates ($\approx 90\%$) against StyleCLIP in out-of-domain manipulation results suggest that our method significantly outperforms StyleCLIP in out-of-domain manipulation.

Quantitative evaluation. We also compare the manipulation performance using the following quality metrics: Directional CLIP similarity ($\mathcal{S}_{dir}$), segmentation-consistency (SC), and face identity similarity (ID). To compute each metric, we use a pretrained CLIP [41], segmentation [63, 67, 68] and face recognition models [15], respectively. Then, during the translation between three attributes in CelebA-HQ (makeup, tanned, gray hair) [27] and LSUN-Church (golden, red brick, sunset) [64], our goal is to achieve the better score in terms of $\mathcal{S}_{dir}$, SC, and ID. As shown in Tab. 3, our method outperforms baselines in all metrics, demonstrating high attribute-correspondence ($\mathcal{S}_{dir}$) as well as well-preservation of identities without unintended changes (SC, ID).

For more experimental details and results of the comparison, see Supplementary Section D and E.

4.2. More Manipulation Results on Other Datasets

Fig. 6 presents more examples of image manipulations on dog face, bedroom and general images using the diffusion models pretrained on AFHQ-Dog-256 [12], LSUN-Bedroom-256 [64] and ImageNet-512 [49] datasets, respectively. The results demonstrate that the reconstruction is nearly flawless and high-resolution images can be flexibly manipulated beyond the boundary of the trained domains. Especially, due to the diversity of the images in ImageNet, GAN-based inversion and its manipulation in the latent space of ImageNet show limited performance [5, 13]. Diffusion-CLIP enables the zero-shot text-driven manipulation of general images, moving a step forward to the general text-driven manipulation. For more results, see Supplementary Section E.

4.3. Image Translation between Unseen Domains

With the fine-tuned diffusion models using Diffusion-CLIP, we can even translate the images in one unseen domain to another unseen domain. Here, we are not required

to collect the images in the source and target domains or introduce external models. In Fig. 7, we perform the image translation results from the portrait artworks and animation images to other unseen domains, Pixar, paintings by Gogh and Neanderthal men. We also show the successful image generation in the unseen domains from the stroke which is the rough image painting with several color blocks. These applications will be useful when enough images for both source and target domains are difficult to collect.

4.4. Noise Combination

As shown in Fig. 8 we can change multiple attributes in one sampling. As discussed before, to perform the multi-attribute transfer, complex loss designs, as well as specific data collection with large manual efforts, aren't required. Finally, Fig. 9 shows that we can control the degree of change of single target attributes according to γ by mixing noises from the original model and the fine-tuned model.

4.5. Dependency on Hyperparameters

In Fig. 10, we show the results of the reconstruction performance depending on S_{for}, S_{gen} when $t_0 = 500$. Even with $S_{for} = 6$, we can see that the reconstruction preserves the identity well. When $S_{for} = 40$, the result of $S_{gen} = 6$ lose some high frequency details, but it's not the degree of ruining the training. When $S_{for} = 200$ and $S_{gen} = 40$, the reconstruction results are so excellent that we cannot differentiate the reconstruction with the result when the original images. Therefore, we just use $(S_{for}, S_{gen}) = (40, 6)$ for the training and $(S_{for}, S_{gen}) = (200, 40)$ for the inference.

We also show the results of manipulation by changing t_0 while fixing other parameters in Fig. 11. In case of skin color changes, 300 is enough. However, in case of the changes with severe shape changes such as the Pixar requires stepping back more as $t_0 = 500$ or $t_0 = 700$. Accordingly, we set different t_0 depending on the attributes. The additional analyses on hyperparameters and ablation studies are provided in Supplementary Section F.

5. Discussion and Conclusion

In this paper, we proposed DiffusionCLIP, a method of text-guided image manipulation method using the pretrained diffusion models and CLIP loss. Thanks to the near-perfect inversion property, DiffusionCLIP has shown excellent performance for both in-domain and out-of-domain manipulation by fine-tuning diffusion models. We also presented several novel applications of using fine-tuned models by combining various sampling strategies.

There are limitations and societal risks on DiffusionCLIP. Therefore, we advise users to make use of our method carefully for proper purposes. Further details on limitations and negative social impacts are given in Supplementary Section G and H.

References

[1] Rameen Abdal, Yipeng Qin, and Peter Wonka. Image2stylegan: How to embed images into the stylegan latent space? In *Proceedings of the IEEE/CVF International Conference on Computer Vision*, pages 4432–4441, 2019. 1, 13, 16

[2] Rameen Abdal, Yipeng Qin, and Peter Wonka. Image2stylegan++: How to edit the embedded images? In *Proceedings of the IEEE/CVF Conference on Computer Vision and Pattern Recognition*, pages 8296–8305, 2020. 1, 13

[3] Yuval Alaluf, Or Patashnik, and Daniel Cohen-Or. Restyle a residual-based stylegan encoder via iterative refinement. In *Proceedings of the IEEE/CVF International Conference on Computer Vision (ICCV)*, October 2021. 1, 2, 6, 7, 13, 16

[4] David Bau, Hendrik Strobelt, William Peebles, Jonas Wulff, Bolei Zhou, Jun-Yan Zhu, and Antonio Torralba. Semantic photo manipulation with a generative image prior. *arXiv preprint arXiv:2005.07727*, 2020. 1, 13

[5] Ashish Bora, Ajil Jalal, Eric Price, and Alexandros G Dimakis. Compressed sensing using generative models. In *International Conference on Machine Learning*, pages 537–546. PMLR, 2017. 2, 8, 12

[6] Andrew Brock, Jeff Donahue, and Karen Simonyan. Large scale gan training for high fidelity natural image synthesis. *arXiv preprint arXiv:1809.11096*, 2018. 2

[7] Andrew Brock, Theodore Lim, James M Ritchie, and Nick Weston. Neural photo editing with introspective adversarial networks. *arXiv preprint arXiv:1609.07093*, 2016. 1, 13

[8] Qifeng Chen and Vladlen Koltun. Photographic image synthesis with cascaded refinement networks. In *Proceedings of the IEEE international conference on computer vision*, pages 1511–1520, 2017. 13

[9] Jooyoung Choi, Sungwon Kim, Yonghyun Jeong, Youngjune Gwon, and Sungroh Yoon. Ilvr: Conditioning method for denoising diffusion probabilistic models. *arXiv preprint arXiv:2108.02938*, 2021. 4, 13, 16

[10] Yunjey Choi, Minje Choi, Munyoung Kim, Jung-Woo Ha, Sunghun Kim, and Jaegul Choo. Stargan: Unified generative adversarial networks for multi-domain image-to-image translation. In *Proceedings of the IEEE conference on computer vision and pattern recognition*, pages 8789–8797, 2018. 5

[11] Yunjey Choi, Youngjung Uh, Jaejun Yoo, and Jung-Woo Ha. Stargan v2: Diverse image synthesis for multiple domains. In *Proceedings of the IEEE/CVF Conference on Computer Vision and Pattern Recognition*, pages 8188–8197, 2020. 5

[12] Yunjey Choi, Youngjung Uh, Jaejun Yoo, and Jung-Woo Ha. Stargan v2: Diverse image synthesis for multiple domains. In *Proceedings of the IEEE Conference on Computer Vision and Pattern Recognition*, 2020. 5, 8, 16, 21

[13] Giannis Daras, Augustus Odena, Han Zhang, and Alexandros G Dimakis. Your local gan: Designing two dimensional local attention mechanisms for generative models. In *Proceedings of the IEEE/CVF Conference on Computer Vision and Pattern Recognition*, pages 14531–14539, 2020. 2, 8, 12

[14] Tali Dekel, Chuang Gan, Dilip Krishnan, Ce Liu, and William T Freeman. Sparse, smart contours to represent and edit images. In *Proceedings of the IEEE Conference on Computer Vision and Pattern Recognition*, pages 3511–3520, 2018. 13

[15] Jiankang Deng, Jia Guo, Niannan Xue, and Stefanos Zafeiriou. Arcface: Additive angular margin loss for deep face recognition. In *Proceedings of the IEEE/CVF Conference on Computer Vision and Pattern Recognition*, pages 4690–4699, 2019. 4, 8, 17, 19

[16] Prafulla Dhariwal and Alex Nichol. Diffusion models beat gans on image synthesis. *arXiv preprint arXiv:2105.05233*, 2021. 2, 3, 4, 13, 16, 17, 18

[17] Laurent Dinh, Jascha Sohl-Dickstein, and Samy Bengio. Density estimation using real nvp. *arXiv preprint arXiv:1605.08803*, 2016. 2

[18] Patrick Esser, Robin Rombach, and Björn Ommer. A note on data biases in generative models. *arXiv preprint arXiv:2012.02516*, 2020. 21

[19] Patrick Esser, Robin Rombach, and Björn Ommer. Taming transformers for high-resolution image synthesis, 2020. 18

[20] Rinon Gal, Or Patashnik, Haggai Maron, Gal Chechik, and Daniel Cohen-Or. Stylegan-nada: Clip-guided domain adaptation of image generators. *arXiv preprint arXiv:2108.00946*, 2021. 2, 3, 6, 7, 13, 16, 17, 20, 21, 22, 23, 24

[21] Ian Goodfellow, Jean Pouget-Abadie, Mehdi Mirza, Bing Xu, David Warde-Farley, Sherjil Ozair, Aaron Courville, and Yoshua Bengio. Generative adversarial nets. *Advances in neural information processing systems*, 27, 2014. 2

[22] Jinjin Gu, Yujun Shen, and Bolei Zhou. Image processing using multi-code gan prior. In *Proceedings of the IEEE/CVF conference on computer vision and pattern recognition*, pages 3012–3021, 2020. 13

[23] Jonathan Ho, Ajay Jain, and Pieter Abbeel. Denoising diffusion probabilistic models. *arXiv preprint arXiv:2006.11239*, 2020. 2, 3, 4, 12, 13, 15

[24] Minyoung Huh, Richard Zhang, Jun-Yan Zhu, Sylvain Paris, and Aaron Hertzmann. Transforming and projecting images into class-conditional generative networks. In *European Conference on Computer Vision*, pages 17–34. Springer, 2020. 13

[25] Phillip Isola, Jun-Yan Zhu, Tinghui Zhou, and Alexei A Efros. Image-to-image translation with conditional adversarial networks. In *Proceedings of the IEEE conference on computer vision and pattern recognition*, pages 1125–1134, 2017. 13

[26] Alexia Jolicoeur-Martineau, Rémi Piché-Taillefer, Rémi Tachet des Combes, and Ioannis Mitliagkas. Adversarial score matching and improved sampling for image generation. *arXiv preprint arXiv:2009.05475*, 2020. 2, 13

[27] Tero Karras, Timo Aila, Samuli Laine, and Jaakko Lehtinen. Progressive growing of gans for improved quality, stability, and variation. *arXiv preprint arXiv:1710.10196*, 2017. 5, 7, 8, 15, 16, 17, 21, 22, 23

[28] Tero Karras, Samuli Laine, and Timo Aila. A style-based generator architecture for generative adversarial networks. In *Proceedings of the IEEE/CVF Conference on Computer Vision and Pattern Recognition*, pages 4401–4410, 2019. 2, 7, 13, 18

[29] Tero Karras, Samuli Laine, Miika Aittala, Janne Hellsten, Jaakko Lehtinen, and Timo Aila. Analyzing and improving the image quality of stylegan. In *Proceedings of the IEEE/CVF Conference on Computer Vision and Pattern Recognition*, pages 8110–8119, 2020. 2, 7, 18

[30] Diederik P Kingma and Prafulla Dhariwal. Glow: Generative flow with invertible 1x1 convolutions. *arXiv preprint arXiv:1807.03039*, 2018. 2

[31] Diederik P Kingma and Max Welling. Auto-encoding variational bayes. *arXiv preprint arXiv:1312.6114*, 2013. 2

[32] Tsung-Yi Lin, Piotr Dollár, Ross Girshick, Kaiming He, Bharath Hariharan, and Serge Belongie. Feature pyramid networks for object detection. In *Proceedings of the IEEE conference on computer vision and pattern recognition*, pages 2117–2125, 2017. 16

[33] Chenlin Meng, Yang Song, Jiaming Song, Jiajun Wu, Jun-Yan Zhu, and Stefano Ermon. Sdedit: Image synthesis and editing with stochastic differential equations. *arXiv preprint arXiv:2108.01073*, 2021. 4, 13, 15, 16

[34] Jacob Menick and Nal Kalchbrenner. Generating high fidelity images with subscale pixel networks and multidimensional upscaling. *arXiv preprint arXiv:1812.01608*, 2018. 2

[35] Clay Mullis and Katherine Crowson. Clip-guided diffusion github repository. In *https://github.com/afiaka87/clip-guided-diffusion*. 18

[36] Alex Nichol and Prafulla Dhariwal. Improved denoising diffusion probabilistic models. *arXiv preprint arXiv:2102.09672*, 2021. 12, 16

[37] Aaron van den Oord, Oriol Vinyals, and Koray Kavukcuoglu. Neural discrete representation learning. *arXiv preprint arXiv:1711.00937*, 2017. 2

[38] Taesung Park, Ming-Yu Liu, Ting-Chun Wang, and Jun-Yan Zhu. Semantic image synthesis with spatially-adaptive normalization. In *Proceedings of the IEEE/CVF Conference on Computer Vision and Pattern Recognition*, pages 2337–2346, 2019. 13

[39] Or Patashnik, Zongze Wu, Eli Shechtman, Daniel Cohen-Or, and Dani Lischinski. Styleclip: Text-driven manipulation of stylegan imagery. *arXiv preprint arXiv:2103.17249*, 2021. 2, 3, 6, 7, 13, 16, 17, 20, 21, 22, 23, 24

[40] Tiziano Portenier, Qiyang Hu, Attila Szabo, Siavash Arjomand Bigdeli, Paolo Favaro, and Matthias Zwicker. Faceshop: Deep sketch-based face image editing. *arXiv preprint arXiv:1804.08972*, 2018. 13

[41] Alec Radford, Jong Wook Kim, Chris Hallacy, Aditya Ramesh, Gabriel Goh, Sandhini Agarwal, Girish Sastry, Amanda Askell, Pamela Mishkin, Jack Clark, et al. Learning transferable visual models from natural language supervision. *arXiv preprint arXiv:2103.00020*, 2021. 2, 3, 8, 13, 17, 18, 21

[42] Prajit Ramachandran, Barret Zoph, and Quoc V Le. Searching for activation functions. *arXiv preprint arXiv:1710.05941*, 2017. 16

[43] Ali Razavi, Aaron van den Oord, and Oriol Vinyals. Generating diverse high-fidelity images with vq-vae-2. In *Advances in neural information processing systems*, pages 14866–14876, 2019. 2

[44] Danilo Rezende and Shakir Mohamed. Variational inference with normalizing flows. In *International conference on machine learning*, pages 1530–1538. PMLR, 2015. 2

[45] Elad Richardson, Yuval Alaluf, Or Patashnik, Yotam Nitzan, Yaniv Azar, Stav Shapiro, and Daniel Cohen-Or. Encoding in style: a stylegan encoder for image-to-image translation. In *Proceedings of the IEEE/CVF Conference on Computer Vision and Pattern Recognition*, pages 2287–2296, 2021. 1, 2, 6, 7, 13, 16

[46] Daniel Roich, Ron Mokady, Amit H Bermano, and Daniel Cohen-Or. Pivotal tuning for latent-based editing of real images. *arXiv preprint arXiv:2106.05744*, 2021. 13

[47] Olaf Ronneberger, Philipp Fischer, and Thomas Brox. U-net: Convolutional networks for biomedical image segmentation. In *International Conference on Medical image computing and computer-assisted intervention*, pages 234–241. Springer, 2015. 4, 15

[48] David E Rumelhart, Geoffrey E Hinton, and Ronald J Williams. Learning internal representations by error propagation. Technical report, California Univ San Diego La Jolla Inst for Cognitive Science, 1985. 4

[49] Olga Russakovsky, Jia Deng, Hao Su, Jonathan Krause, Sanjeev Satheesh, Sean Ma, Zhiheng Huang, Andrej Karpathy, Aditya Khosla, Michael Bernstein, Alexander C. Berg, and Li Fei-Fei. ImageNet Large Scale Visual Recognition Challenge. *International Journal of Computer Vision (IJCV)*, 115(3):211–252, 2015. 2, 8, 12, 13, 15, 16, 18, 21, 25, 26, 27

[50] Yujun Shen, Ceyuan Yang, Xiaoou Tang, and Bolei Zhou. Interfacegan: Interpreting the disentangled face representation learned by gans. *IEEE transactions on pattern analysis and machine intelligence*, 2020. 18

[51] Jascha Sohl-Dickstein, Eric Weiss, Niru Maheswaranathan, and Surya Ganguli. Deep unsupervised learning using nonequilibrium thermodynamics. In *International Conference on Machine Learning*, pages 2256–2265. PMLR, 2015. 2, 13

[52] Jiaming Song, Chenlin Meng, and Stefano Ermon. Denoising diffusion implicit models. *arXiv preprint arXiv:2010.02502*, 2020. 2, 3, 4, 13, 14

[53] Yang Song and Stefano Ermon. Generative modeling by estimating gradients of the data distribution. *arXiv preprint arXiv:1907.05600*, 2019. 2, 13

[54] Yang Song, Jascha Sohl-Dickstein, Diederik P Kingma, Abhishek Kumar, Stefano Ermon, and Ben Poole. Score-based generative modeling through stochastic differential equations. *arXiv preprint arXiv:2011.13456*, 2020. 2, 13

[55] Omer Tov, Yuval Alaluf, Yotam Nitzan, Or Patashnik, and Daniel Cohen-Or. Designing an encoder for stylegan image manipulation. *ACM Transactions on Graphics (TOG)*, 40(4):1–14, 2021. 1, 2, 6, 7, 13, 16, 18

[56] Aaron Van Oord, Nal Kalchbrenner, and Koray Kavukcuoglu. Pixel recurrent neural networks. In *International Conference on Machine Learning*, pages 1747–1756. PMLR, 2016. 2

[57] Ashish Vaswani, Noam Shazeer, Niki Parmar, Jakob Uszkoreit, Llion Jones, Aidan N Gomez, Łukasz Kaiser, and Illia Polosukhin. Attention is all you need. In *Advances in neural information processing systems*, pages 5998–6008, 2017. 4, 16

[58] Tengfei Wang, Yong Zhang, Yanbo Fan, Jue Wang, and Qifeng Chen. High-fidelity gan inversion for image attribute editing. *arXiv preprint arXiv:2109.06590*, 2021. 6, 13, 16

[59] Ting-Chun Wang, Ming-Yu Liu, Jun-Yan Zhu, Andrew Tao, Jan Kautz, and Bryan Catanzaro. High-resolution image synthesis and semantic manipulation with conditional gans. In *Proceedings of the IEEE conference on computer vision and pattern recognition*, pages 8798–8807, 2018. 13

[60] Yuxin Wu and Kaiming He. Group normalization. In *Proceedings of the European conference on computer vision (ECCV)*, pages 3–19, 2018. 16

[61] Zongze Wu, Dani Lischinski, and Eli Shechtman. Stylespace analysis: Disentangled controls for stylegan image generation. In *Proceedings of the IEEE/CVF Conference on Computer Vision and Pattern Recognition*, pages 12863–12872, 2021. 13, 18

[62] Weihao Xia, Yujiu Yang, Jing-Hao Xue, and Baoyuan Wu. Tedigan: Text-guided diverse face image generation and manipulation. In *Proceedings of the IEEE/CVF Conference on Computer Vision and Pattern Recognition*, pages 2256–2265, 2021. 6

[63] Changqian Yu, Jingbo Wang, Chao Peng, Changxin Gao, Gang Yu, and Nong Sang. Bisenet: Bilateral segmentation network for real-time semantic segmentation. In *Proceedings of the European conference on computer vision (ECCV)*, pages 325–341, 2018. 8, 17

[64] Fisher Yu, Yinda Zhang, Shuran Song, Ari Seff, and Jianxiong Xiao. Lsun: Construction of a large-scale image dataset using deep learning with humans in the loop. *arXiv preprint arXiv:1506.03365*, 2015. 2, 5, 7, 8, 13, 15, 17, 21

[65] Sergey Zagoruyko and Nikos Komodakis. Wide residual networks. *arXiv preprint arXiv:1605.07146*, 2016. 15

[66] Richard Zhang, Phillip Isola, Alexei A Efros, Eli Shechtman, and Oliver Wang. The unreasonable effectiveness of deep features as a perceptual metric. In *CVPR*, 2018. 6

[67] Bolei Zhou, Hang Zhao, Xavier Puig, Sanja Fidler, Adela Barriuso, and Antonio Torralba. Scene parsing through ade20k dataset. In *Proceedings of the IEEE Conference on Computer Vision and Pattern Recognition*, 2017. 8, 17

[68] Bolei Zhou, Hang Zhao, Xavier Puig, Tete Xiao, Sanja Fidler, Adela Barriuso, and Antonio Torralba. Semantic understanding of scenes through the ade20k dataset. *International Journal on Computer Vision*, 2018. 8, 17

[69] Jiapeng Zhu, Yujun Shen, Deli Zhao, and Bolei Zhou. In-domain gan inversion for real image editing. In *European conference on computer vision*, pages 592–608. Springer, 2020. 7, 13, 18

[70] Jun-Yan Zhu, Philipp Krähenbühl, Eli Shechtman, and Alexei A Efros. Generative visual manipulation on the natural image manifold. In *European conference on computer vision*, pages 597–613. Springer, 2016. 13

[71] Jun-Yan Zhu, Taesung Park, Phillip Isola, and Alexei A Efros. Unpaired image-to-image translation using cycle-consistent adversarial networks. In *Proceedings of the IEEE international conference on computer vision*, pages 2223–2232, 2017. 13

[72] Peihao Zhu, Rameen Abdal, Yipeng Qin, and Peter Wonka. Sean: Image synthesis with semantic region-adaptive normalization. In *Proceedings of the IEEE/CVF Conference on Computer Vision and Pattern Recognition*, pages 5104–5113, 2020. 13
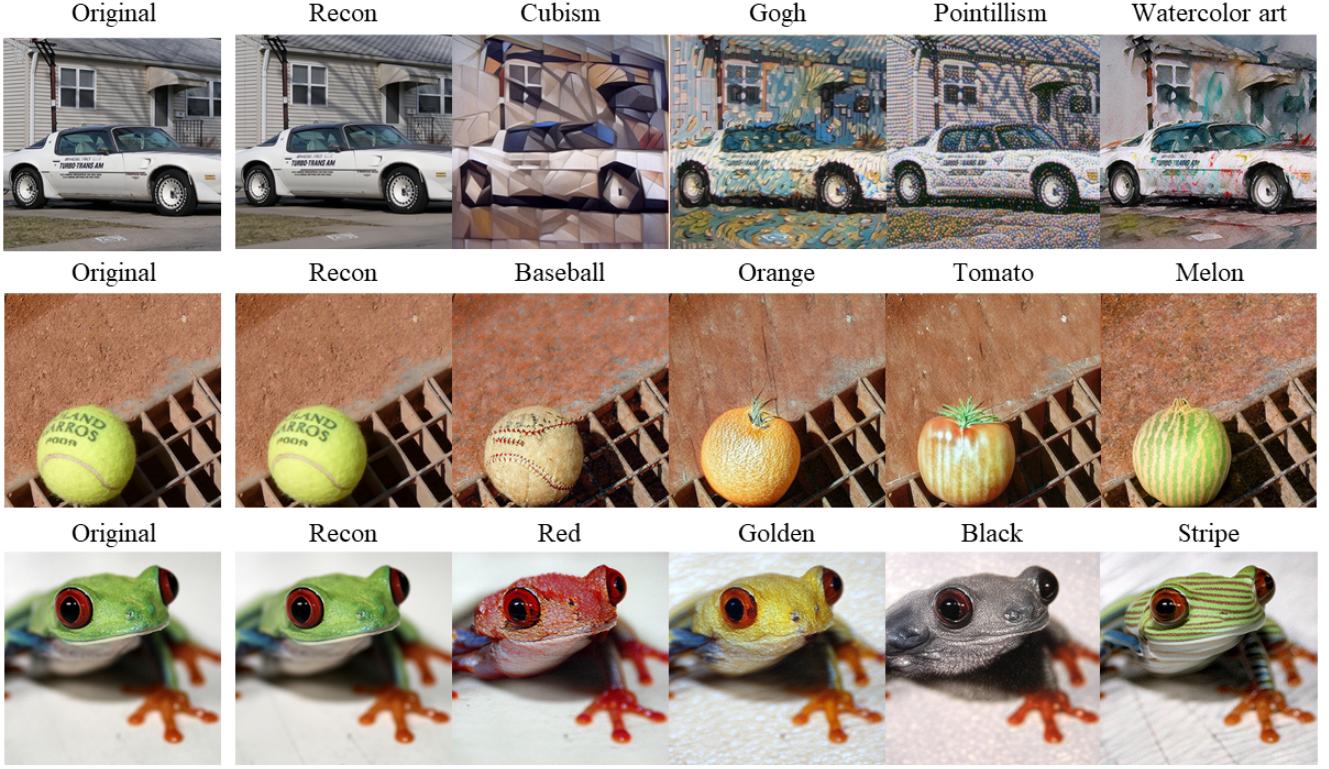
Original	Recon	Cubism	Gogh	Pointillism	Watercolor art

Original	Recon	Baseball	Orange	Tomato	Melon

Original	Recon	Red	Golden	Black	Stripe

Figure 12. DiffusionCLIP can even perform manipulation of 512×512 images using the ImageNet [49] pretrained diffusion models. Thanks to the near-perfect inversion capability, DiffusionCLIP enables the zero-shot text-driven manipulation, moving a step forward to the general text-driven manipulation. In contrast, due to the diversity of the images in ImageNet, GAN-based inversion and its manipulation in the latent space of ImageNet shows limited performance [5, 13]. Hence, zero-shot text-driven manipulation using ImageNet pretrained GAN have been rarely explored. For more results, see Fig. 18, 28, 29 and 30.

Supplementary Material

A. Details on Related Works

A.1. DDPM, DDIM and ODE Approximation

Denoising diffusion probabalistic models (DDPM). Diffusion probabilistic models [23] are a class of latent variable models based on forward and reverse processes. Suppose that our model distribution $p_\theta(\boldsymbol{x}_0)$ tries to approximate a data distribution $q(\boldsymbol{x}_0)$. Let $\mathcal{X}$ denote the sample space for $\boldsymbol{x}_0$ generated from a sequence of latent variables $\boldsymbol{x}_t$ for $t = 1, \cdots, T$, where $\boldsymbol{x}_T \sim \mathcal{N}(\boldsymbol{0}, \mathbf{I})$. In the forward process, noises are gradually added to data $\boldsymbol{x}_0$ and the latent sequence set $\boldsymbol{x}_{1:T}$ are generated through the following Markov chain upon a variance schedule defined by $\{\beta_t\}_{t=1}^T$:

$$q(\boldsymbol{x}_{1:T}) := \prod_{t=1}^T q(\boldsymbol{x}_t | \boldsymbol{x}_{t-1}), \quad (16)$$

where

$$q(\boldsymbol{x}_t | \boldsymbol{x}_{t-1}) := \mathcal{N}(\sqrt{1-\beta_t}\boldsymbol{x}_{t-1}, \beta_t \mathbf{I}). \quad (17)$$

Then, $q(\boldsymbol{x}_t | \boldsymbol{x}_0)$ can be represented in a closed form as $q(\boldsymbol{x}_t | \boldsymbol{x}_0) = \mathcal{N}(\boldsymbol{x}_t; \sqrt{\alpha_t}\boldsymbol{x}_0, (1 - \alpha_t)\mathbf{I})$, where $\alpha_t := 1 - \beta_t$ and $\bar{\alpha}_t := \prod_{s=1}^t (1 - \beta_s)$. Then, we can sample $\boldsymbol{x}_t$ as:

$$\boldsymbol{x}_t = \sqrt{\bar{\alpha}_t}\boldsymbol{x}_0 + \sqrt{1 - \bar{\alpha}_t}\boldsymbol{w}, \text{ where } \boldsymbol{w} \sim \mathcal{N}(\boldsymbol{0}, \mathbf{I}). \quad (18)$$

In the reverse process, $\boldsymbol{x}_T$ is denoised to generate $\boldsymbol{x}_0$ through the following Markov process:

$$p_\theta(\boldsymbol{x}_{0:T}) := p(\boldsymbol{x}_T) \prod_{t=1}^T p_\theta(\boldsymbol{x}_{t-1} | \boldsymbol{x}_t), \quad (19)$$

where $\boldsymbol{x}_T \sim \mathcal{N}(\boldsymbol{0}, \mathbf{I})$ and

$$p_\theta(\boldsymbol{x}_{t-1} | \boldsymbol{x}_t) := \mathcal{N}(\boldsymbol{\mu}_\theta(\boldsymbol{x}_t, t), \boldsymbol{\Sigma}_\theta(\boldsymbol{x}_t, t)\mathbf{I}), \quad (20)$$

where $\boldsymbol{\Sigma}_\theta(\boldsymbol{x}_t, t)$ is set to be learnable to improve the sample quality [36] and

$$\boldsymbol{\mu}_\theta(\boldsymbol{x}_t, t) = \frac{1}{\sqrt{\alpha_t}}\left(\boldsymbol{x}_t - \frac{1 - \alpha_t}{\sqrt{1 - \bar{\alpha}_t}}\boldsymbol{\epsilon}_\theta(\boldsymbol{x}_t, t)\right). \quad (21)$$

and the neural network $\boldsymbol{\epsilon}_\theta(\boldsymbol{x}_t, t)$ is trained with the following improved objective [23]:

$$\mathcal{L}_{\text{simple}} := \mathbb{E}_{\boldsymbol{x}_0, \boldsymbol{w}, t} ||\boldsymbol{w} - \boldsymbol{\epsilon}_\theta(\sqrt{\bar{\alpha}_t}\boldsymbol{x}_0 + \sqrt{1 - \bar{\alpha}_t}\boldsymbol{w}, t)||_2^2, \quad (22)$$

where $\boldsymbol{w} \sim \mathcal{N}(\boldsymbol{0}, \mathbf{I})$.

12

Denoising diffusion implicit models (DDIM). An alternative non-Markovian forward process that has the same forward marginals as DDPM and corresponding sampling process is proposed in [52]. Here, the forward diffusion is described by

$$\boldsymbol{x}_t = \sqrt{\bar{\alpha}_t}\boldsymbol{x}_0 + \sqrt{1 - \bar{\alpha}_t}\boldsymbol{z},$$

while the reverse diffusion can be represented as following:

$$\boldsymbol{x}_{t-1} = \sqrt{\bar{\alpha}_{t-1}}\boldsymbol{f}_\theta(\boldsymbol{x}_t, t) + \sqrt{1 - \bar{\alpha}_{t-1} - \sigma_t^2}\boldsymbol{\epsilon}_\theta(\boldsymbol{x}_t, t) + \sigma_t^2\boldsymbol{z}, \tag{23}$$

where $\boldsymbol{z} \sim \mathcal{N}(\boldsymbol{0}, \mathbf{I})$ and $\boldsymbol{f}_\theta(\boldsymbol{x}_t, t)$ is a the prediction of $\boldsymbol{x}_0$ at t given $\boldsymbol{x}_t$:

$$\boldsymbol{f}_\theta(\boldsymbol{x}_t, t) := \frac{\boldsymbol{x}_t - \sqrt{1 - \bar{\alpha}_t}\boldsymbol{\epsilon}_\theta(\boldsymbol{x}_t, t)}{\sqrt{\bar{\alpha}_t}}, \tag{24}$$

and $\boldsymbol{\epsilon}_\theta(\boldsymbol{x}_t, t)$ is computed by (22).

This sampling allows using different reverse samplers by changing the variance of the reverse noise σ_t. Especially, by setting this noise to 0, which is a DDIM sampling process [52], the sampling process becomes deterministic, enabling to conversation latent variables into the data consistently and to sample with fewer steps.

ODE approximation. In fact, DDIM can be considered as a Euler method to solve ODE. Specifically, Eq. (23) can be represented as:

$$\sqrt{\frac{1}{\bar{\alpha}_{t-1}}}\boldsymbol{x}_{t-1} - \sqrt{\frac{1}{\bar{\alpha}_t}}\boldsymbol{x}_t = \left(\sqrt{\frac{1}{\bar{\alpha}_{t-1}} - 1} - \sqrt{\frac{1}{\bar{\alpha}_t} - 1}\right)\boldsymbol{\epsilon}_\theta(\boldsymbol{x}_t, t) \tag{25}$$

If we set $\boldsymbol{y}_t := \sqrt{1/\bar{\alpha}_t}\boldsymbol{x}_t$ and $p_t := \sqrt{1/\bar{\alpha}_t - 1}$, we can rewrite Eq. (25) as follows:

$$\boldsymbol{y}_{t-1} - \boldsymbol{y}_t = (p_{t-1} - p_t)\boldsymbol{\epsilon}_\theta(\boldsymbol{x}_t, t). \tag{26}$$

In the limit of small steps, this equation goes to ODE

$$d\boldsymbol{y}_t = \boldsymbol{\epsilon}_\theta(\boldsymbol{x}_t, t)dp_t.$$

Then, the reversal of this ODE can be derived as follows:

$$\boldsymbol{y}_{t+1} - \boldsymbol{y}_t = (p_{t+1} - p_t)\boldsymbol{\epsilon}_\theta(\boldsymbol{x}_t, t), \tag{27}$$

which becomes:

$$\sqrt{\frac{1}{\bar{\alpha}_{t+1}}}\boldsymbol{x}_{t+1} - \sqrt{\frac{1}{\bar{\alpha}_t}}\boldsymbol{x}_t = \left(\sqrt{\frac{1}{\bar{\alpha}_{t+1}} - 1} - \sqrt{\frac{1}{\bar{\alpha}_t} - 1}\right)\boldsymbol{\epsilon}_\theta(\boldsymbol{x}_t, t). \tag{28}$$

Finally, the above equation can be written as:

$$\boldsymbol{x}_{t+1} = \sqrt{\bar{\alpha}_{t+1}}\boldsymbol{f}_\theta(\boldsymbol{x}_t, t) + \sqrt{1 - \bar{\alpha}_{t+1}}\boldsymbol{\epsilon}_\theta(\boldsymbol{x}_t, t), \tag{29}$$

which is equal to our forward DDIM process formulation that is used in Sec. 3.2.

A.2. Additional Related Works

Diffusion-based image manipulation. Recent diffusion models have demonstrated impressive performance in image generation [16, 23, 26, 51–54] with additional advantages of great mode coverage and stable training.

Despite this recent progress, only a few studies [9, 33] have been carried out for image manipulation with diffusion models, such as local editing and the image translation from unseen domain to the trained domain. In ILVR [9], image translation where the low-frequency component of the reference image is conditioned at each transition during the sampling process is introduced. In SDEdit [33], images with the user's local edit or strokes are first noised via the stochastic SDE process, and subsequently denoised by simulating the reverse SDE to generate the realistic image in the pretrained domain. However, it is not clear how these methods can be extended for more general image manipulation applications, such as attribute manipulation, translation from the trained domain to multiple unseen domains, etc.

On the other hand, DiffusionCLIP enables text-guided image manipulation with an infinite number of types of text-driven attributes, and translation of images in the pretrained or an unseen domain to another unseen domain.

GAN-based image manipulation. Image manipulation methods have been mostly implemented using GAN models. Conditional GAN methods [8, 14, 25, 38, 40, 59, 71, 72] learn direct mappings from original images to target images. However, these methods need additional training and collection of the dataset with a huge amount of manual effort whenever the new controls are necessary.

In GAN inversion based methods [1–4, 7, 22, 45, 46, 55, 58, 61, 69, 70], an input image is first converted to a latent vector so that the image can be manipulated by modifying the latent or fine-tuning the generator. In recent works [20, 39], GAN inversion is combined with the CLIP loss [41], so that image manipulation given simple text prompts can be achieved without additional training dataset for target distribution.

However, image manipulation by GAN inversion still demands further investigation, because many datasets are still hard to invert due to the limited inversion capability of GAN models [24, 28, 45]. Even the encoder-based GAN inversion approaches [3, 45, 55], which is the current state-of-the-art (SOTA) methods, often fail to reconstruct images with novel poses, views, and details, inducing the unintended change in the manipulation results. This issue becomes even worse in the case of images from a dataset with high variances such as church images in LSUN Church [64] or ImageNet dataset [49].

On the other hand, DiffusionCLIP allows near-perfect inversions, so that it can perform zero-shot text-driven image manipulation successfully, preserving important details even

for images from a dataset with high variance. We can even translate the image from an unseen domain into another unseen domain or generate images in an unseen domain from the strokes. In the following, we illustrate the detailed procedure with pseudocode.

B. Details on Methods

B.1. DiffusionCLIP Fine-tuning

We adopt a two-step approach as detailed in Algorithm 1. First, real images or sampled images from pretrained domain $\{x_0^{(i)}\}_{i=1}^N$ are inverted to the latents $\{x_{t_0}^{(i)}\}_{i=1}^N$ via deterministic forward DDIM processes [52] with the pretrained diffusion model ϵ_θ. To accelerate the process, instead of performing forward diffusion until the last time step T, we use fewer discretization steps $\{\tau_s\}_{s=1}^{S_{\text{for}}}$ such that $\tau_1 = 0, \tau_{S_{\text{for}}} = t_0$.

In the second step, we start to update $\epsilon_{\hat\theta}$, a copy of the pretrained diffusion model. For each latent in $\{x_{t_0}^{(i)}\}_{i=1}^N$, the image is sampled through the reverse DDIM process [52] and the model is updated guided by CLIP loss $\mathcal{L}_{\text{direction}}$ and identity loss $\mathcal{L}_{\text{ID}}$ to generate images that represent y_{tar}. The second step is repeated K times until converged.

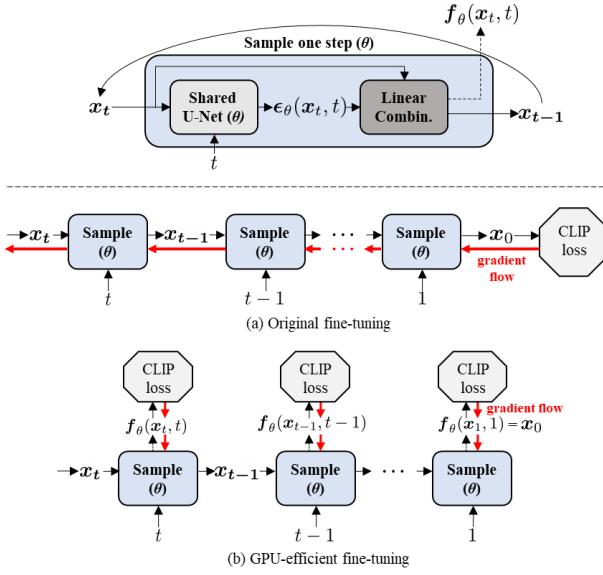

(a) Original fine-tuning

(b) GPU-efficient fine-tuning

Figure 13. Gradient flows during the fine-tuning and GPU-efficient fine-tuning. In GPU-efficient fine-tuning, loss calculation and a gradient step are proceeded at each time step t with $f_\theta(x_t, t)$, the prediction of x_0 at t.

GPU-efficient fine-tuning. During the fine-tuning, the model is updated by back-propagating the gradient from the last step as illustrated in Fig. 13(a) and Algorithm 2. Although this method shows great manipulation performance, as the gradient pass the model S_{gen} times, the GPU usage can be burdensome. Therefore, we additionally propose GPU-efficient fine-tuning method. Here, as shown in in Fig. 13(b),

---

Algorithm 1: DiffuisonCLIP fine-tuning

Input: ϵ_θ (pretrained model), $\{x_0^{(i)}\}_{i=1}^N$ (images to precompute), y_{ref} (reference text), y_{tar} (target text), t_0 (return step), S_{for} (# of inversion steps), S_{gen}(# of generation steps), K (# of fine-tuning iterations)

Output: $\epsilon_{\hat\theta}$ (fine-tuned model)

```
// Step 1:  Precompute latents
```
1 Define $\{\tau_s\}_{s=1}^{S_{\text{for}}}$ s.t. $\tau_1 = 0, \tau_{S_{\text{for}}} = t_0$.
2 **for** $i = 1, 2, \ldots, N$ **do**
3   **for** $s = 1, 2, \ldots, S_{\text{for}} - 1$ **do**
4         $\epsilon \leftarrow \epsilon_\theta(x_{\tau_s}^{(i)}, \tau_s);\ \ f \leftarrow f_\theta(x_{\tau_s}^{(i)}, \tau_s)$
5         $x_{\tau_{s+1}}^{(i)} \leftarrow \sqrt{\alpha_{\tau_{s+1}}}f + \sqrt{1 - \alpha_{\tau_{s+1}}}\epsilon$
6   Save the latent $x_{t_0}^{(i)} = x_{\tau_{S_{\text{for}}}}^{(i)}$.
```
// Step 2:  Update the diffusion model
```
7 Clone the pretrained model $\epsilon_{\hat\theta} \leftarrow \epsilon_\theta$
8 Define $\{\tau_s\}_{s=1}^{S_{\text{gen}}}$ s.t. $\tau_1 = 0, \tau_{S_{\text{gen}}} = t_0$.
9 **for** $k = 1, 2, \ldots, K$ **do**
10   **for** $i = 1, 2, \ldots, N$ **do**
11   Clone the latent $\hat{x}_{t_0}^{(i)} \leftarrow x_{t_0}^{(i)}$.
12   **for** $s = S_{\text{gen}}, S_{\text{gen}} - 1, \ldots, 2$ **do**
13             $\epsilon \leftarrow \epsilon_{\hat\theta}(\hat{x}_{\tau_s}^{(i)}, \tau_s);\ \ f \leftarrow f_{\hat\theta}(\hat{x}_{\tau_s}^{(i)}, \tau_s)$
14             $\hat{x}_{\tau_{s-1}}^{(i)} \leftarrow \sqrt{\alpha_{\tau_{s-1}}}f + \sqrt{1 - \alpha_{\tau_{s-1}}}\epsilon$
15         $\mathcal{L}_{\text{total}} \leftarrow \mathcal{L}_{\text{direction}}(\hat{x}_0^{(i)}, y_{\text{tar}}; x_0^{(i)}, y_{\text{ref}})$
16         $\mathcal{L}_{\text{total}} \leftarrow \mathcal{L}_{\text{total}} + \mathcal{L}_{\text{id}}(\hat{x}_0^{(i)}, x_0^{(i)})$
17   Take a gradient step on $\nabla_{\hat\theta}\mathcal{L}_{\text{total}}$.

Algorithm 2: GPU-efficient fine-tuning

```
// Step 2:  Update the diffusion model
```
1 Clone the pretrained model $\epsilon_{\hat\theta} \leftarrow \epsilon_\theta$
2 Define $\{\tau_s\}_{s=1}^{S_{\text{gen}}}$ s.t. $\tau_1 = 0, \tau_{S_{\text{gen}}} = t_0$.
3 **for** $k = 1, 2, \ldots, K$ **do**
4   **for** $i = 1, 2, \ldots, N$ **do**
5   Clone the latent $\hat{x}_{t_0}^{(i)} \leftarrow x_{t_0}^{(i)}$.
6   **for** $s = S_{\text{gen}}, S_{\text{gen}} - 1, \ldots, 2$ **do**
7             $\epsilon \leftarrow \epsilon_{\hat\theta}(\hat{x}_{\tau_s}^{(i)}, \tau_s);\ \ f \leftarrow f_{\hat\theta}(\hat{x}_{\tau_s}^{(i)}, \tau_s)$
8             $\hat{x}_{\tau_{s-1}}^{(i)} \leftarrow \sqrt{\alpha_{s-1}}f + \sqrt{1 - \alpha_{s-1}}\epsilon$
9             $\mathcal{L}_{\text{total}} \leftarrow \mathcal{L}_{\text{direction}}(f, y_{\text{tar}}; x_0^{(i)}, y_{\text{ref}})$
10            $\mathcal{L}_{\text{total}} \leftarrow \mathcal{L}_{\text{total}} + \mathcal{L}_{\text{id}}(f, x_0^{(i)})$
11   Take a gradient step on $\nabla_{\hat\theta}\mathcal{L}_{\text{total}}$.

---

the back-propagation from the loss functions is performed at each time step t. GPU-efficient fine-tuning can require half of VRAM usage compared to the original fine-tuning, but

it requires twice as much time due to calculating loss and making steps at each time step. More details of running time can be found in Sec. G. We show the result of manipulating ImageNet [49] 512×512 images using GPU-efficient fine-tuning method in Fig. 18, 28, 29 and 30.

Image manipulation via fine-tuned model. Once the diffusion model $\epsilon_{\hat{\theta}}$ is fine-tuned for the target control y_{tar}, the manipulation process of a input image x_0 is quite simple as in Algorithm 3. Specifically, x_0 is inverted to x_{t_0} through the forward DDIM process with the original pretrained model ϵ_θ, followed by the reverse DDIM process with the fine-tuned model $\epsilon_{\hat{\theta}}$ resulting $\hat{x}_0$. We use the same t_0 as used in the fine-tuning.

Algorithm 3: DiffuisonCLIP manipulation

Input: x_0 (input image), $\epsilon_{\hat{\theta}}$ (fine-tuned model), ϵ_θ (pretrained model), t_0 (return step), S_{for} (# of inversion steps), S_{gen}(# of generation steps)

1 **Function** Manipulation(x_0, $\epsilon_{\hat{\theta}}$, *)**:**
2 $\quad$ Define $\{\tau_s\}_{s=1}^{S_{\text{for}}}$ s.t. $\tau_1 = 0, \tau_{S_{\text{for}}} = t_0$.
3 $\quad$ **for** $s = 1, 2, \ldots, S_{\text{for}} - 1$ **do**
4 $\quad\quad$ $\epsilon \leftarrow \epsilon_\theta(x_{\tau_s}, \tau_s); \quad f \leftarrow f_\theta(x_{\tau_s}, \tau_s)$
5 $\quad\quad$ $x_{\tau_{s+1}} \leftarrow \sqrt{\alpha_{\tau_{s+1}}} f + \sqrt{1 - \alpha_{\tau_{s+1}}} \epsilon$
6 $\quad$ Define $\{\tau_s\}_{s=1}^{S_{\text{gen}}}$ s.t. $\tau_1 = 0, \tau_{S_{\text{gen}}} = t_0$
7 $\quad$ $\hat{x}_{t_0} \leftarrow x_{t_0}$
8 $\quad$ **for** $s = S_{\text{gen}}, S_{\text{gen}} - 1, \ldots, 2$ **do**
9 $\quad\quad$ $\epsilon \leftarrow \epsilon_{\hat{\theta}}(\hat{x}_{\tau_s}, \tau_s); \quad f \leftarrow f_{\hat{\theta}}(\hat{x}_{\tau_s}, \tau_s)$
10 $\quad\quad$ $\hat{x}_{\tau_{s-1}} \leftarrow \sqrt{\alpha_{\tau_{s-1}}} f + \sqrt{1 - \alpha_{\tau_{s-1}}} \epsilon$
11 $\quad$ **return** $\hat{x}_0$ (manipulated image)

B.2. Image Translation between Unseen Domains

By combining the method in SDEdit [33] and the manipulation with the fine-tuned model by DiffusionCLIP as detailed in Algorithm 4, we can even translate an image from an unseen domain into another unseen domain. In the first step, the input image in the source unseen domain x_0 is first perturbed to x'_{t_0} through the stochastic forward DDPM process [23] until the return step t_0. Next, the image in the pretrained domain x'_0 is sampled through the reverse DDIM process with the original pretrained model ϵ_θ. These forward-generative processes are repeated for K_{DDPM} times until the image x'_0 is close to the image in the pretrained domain.

In the second step, x'_0 is manipulated into the image $\hat{x}_0$ in the CLIP-guided unseen domain with the fine-tuned model $\epsilon_{\hat{\theta}}$ as in Algorithm 3.

Algorithm 4: Translation between unseen domains

Input: x_0 (image in an unseen domain or stroke), $\epsilon_{\hat{\theta}}$ (fine-tuned model), K_{DDPM} (# of iterations of Step 1), ϵ_θ (pretrained model), t_0 (return step), S_{for} (# of inversion steps), S_{gen}(# of generation steps)

Output: $\hat{x}_0$ (manipulated image)

`// Step 1:  Source unseen → Pretrained`
1 Define $\{\tau_s\}_{s=1}^{S_{\text{gen}}}$ s.t. $\tau_1 = 0, \tau_{S_{\text{gen}}} = t_0$.
2 $x'_0 \leftarrow x_0$
3 **for** $k = 1, 2, \ldots, K_{\text{DDPM}}$ **do**
4 $\quad$ $w \sim \mathcal{N}(0, I)$
5 $\quad$ $x'_{t_0} \leftarrow \sqrt{\alpha_{t_0}} x'_0 + \sqrt{1 - \alpha_{t_0}} w$
6 $\quad$ **for** $s = S_{\text{gen}}, S_{\text{gen}} - 1, \ldots, 2$ **do**
7 $\quad\quad$ $\epsilon \leftarrow \epsilon_\theta(x'_{\tau_s}, \tau_s); \quad f \leftarrow f_\theta(x'_{\tau_s}, \tau_s)$
8 $\quad\quad$ $x'_{\tau_{s-1}} \leftarrow \sqrt{\alpha_{\tau_{s-1}}} f + \sqrt{1 - \alpha_{\tau_{s-1}}} \epsilon$

`// Step 2:  Pretrained → Target unseen`
9 $\hat{x}_0 \leftarrow$ Manipulation(x'_0, $\epsilon_{\hat{\theta}}$, *)

B.3. Noise Combination

With the multiple diffusion models fine-tuned for the different controls $\{\epsilon_{\hat{\theta}_i}\}_{i=1}^M$, we can change multiple attributes through only one sampling process. Specifically, we can flexibly mix several single attribute fine-tuned models with different combinations as described in Algorithm 5, without having to fine-tune new models with target texts that define multiple attributes.

More specifically, we first invert an input image x_0 into x_{t_0} via the forward DDIM process with the original pretrained diffusion model ϵ_θ as single attribute manipulation. Then, we use the multiple fine-tuned models during the reverse DDIM process. By applying different time dependent weight $\gamma_i(t)$ satisfying $\sum_{i=1}^M \gamma_i(t) = 1$ for each model, we can control the degree of change for multiple attributes. Of note, we can also apply this noise combination method for controlling the degree of change during single attribute manipulation. By mixing the noise from the original pretrained model ϵ_θ and the fine-tuned model $\epsilon_{\hat{\theta}}$ concerning a single γ, we can perform interpolation between the original image and the manipulated image smoothly.

C. Details on Network

Most of existing diffusion models receives x_t and t as inputs to the network $\epsilon_\theta(x_t, t)$. We use the DDPM [23] models pre-trained on 256×256 images in CelebA-HQ [27], LSUN-Bedroom and LSUN-Church [64] datasets. This model adopts the U-Net [47] architecture based on Wide-ResNet [65] shared across t as represented in Fig. 14. In specific, the model is composed of the encoder part, middle part, decoder part, and time embedding part. In the encoder

Algorithm 5: Multi-attribute transfer

Input: $\boldsymbol{x}_0$ (input image), $\{\boldsymbol{\epsilon}_{\hat{\theta}_i}\}_{i=1}^M$ (multiple fine-tuned models), $\boldsymbol{\epsilon}_\theta$ (pretrained model), $\{\gamma(t)_i\}_{i=1}^M$ (sequence of model weights), t_0 (return step), S_{for} (# of inversion steps), S_{gen}(# of generation steps)

Output: $\hat{\boldsymbol{x}}_0$ (manipulated image)

1   Define $\{\tau_s\}_{s=1}^{S_{\text{for}}}$ s.t. $\tau_1 = 0, \tau_{S_{\text{for}}} = t_0$.
2   **for** $s = 1, 2, \ldots, S_{\text{for}} - 1$ **do**
3     $\boldsymbol{\epsilon} \leftarrow \boldsymbol{\epsilon}_\theta(\boldsymbol{x}_{\tau_s}, \tau_s); \; \boldsymbol{f} \leftarrow \boldsymbol{f}_\theta(\boldsymbol{x}_{\tau_s}, \tau_s)$
4     $\boldsymbol{x}_{\tau_{s+1}} \leftarrow \sqrt{\alpha_{\tau_{s+1}}}\boldsymbol{f} + \sqrt{1 - \alpha_{\tau_{s+1}}}\boldsymbol{\epsilon}$
5   Define $\{\tau_s\}_{s=1}^{S_{\text{gen}}}$ s.t. $\tau_1 = 0, \tau_{S_{\text{gen}}} = t_0$.
6   $\hat{\boldsymbol{x}}_{t_0} \leftarrow \boldsymbol{x}_{t_0}$
7   **for** $s = S_{\text{gen}}, S_{\text{gen}} - 1, \ldots, 2$ **do**
8     $\boldsymbol{\epsilon} \leftarrow \sum_{i=1}^M \gamma_i(\tau_s)\boldsymbol{\epsilon}_{\hat{\theta}_i}(\hat{\boldsymbol{x}}_{\tau_s}, \tau_s)$
9     $\boldsymbol{f} \leftarrow \sum_{i=1}^M \gamma_i(\tau_s)\boldsymbol{f}_{\hat{\theta}_i}(\hat{\boldsymbol{x}}_{\tau_s}, \tau_s)$
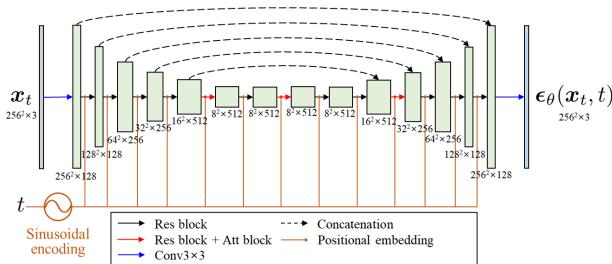10 $\hat{\boldsymbol{x}}_{\tau_{s-1}} \leftarrow \sqrt{\alpha_{\tau_{s-1}}}\boldsymbol{f} + \sqrt{1 - \alpha_{\tau_{s-1}}}\boldsymbol{\epsilon}$

Figure 14. The shared U-Net architecture across t of the diffusion model that generates 256×256 images. The model receives $\boldsymbol{x}_t$ and t as inputs and outputs $\boldsymbol{\epsilon}_\theta(\boldsymbol{x}_t, t)$.
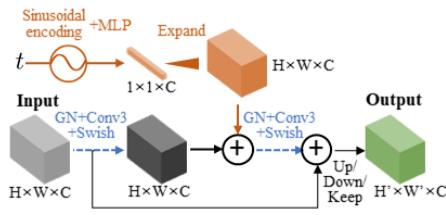

Figure 15. Details of Res block.

part, the 8×8 feature is generated from the 256×256 input image via 1 input convolution and 5 Res blocks. One Res block is composed of two convolutional blocks including Group normalization [60] and Swish activation [42] with the residual connection as in Fig. 15. At the 16×16 resolution, self-attention blocks are added to the Res block. The middle part consists of 3 Res blocks and the second block includes a self-attention block. In the decoder part, the output whose resolution is the same as the input is produced from the feature after the middle part through 5 Res blocks and 1 output convolution with skip connections from the features

in the encoder part. In the time embedding part, the diffusion time t is embedded into each Res blocks as represented in Fig. 15 after the Transformer sinusoidal encoding as proposed in [57]. We use the models pretrained on Celeba-HQ, LSUN-Bedroom, and LSUN-Church models that are used in [33].

For the manipulation of dog faces, we use the improved DDPM [36] models pre-trained on AFHQ-Dog [12]. The architecture is almost same except that the model produces the extra outputs at the output convolution to predict the variance $\boldsymbol{\Sigma}_\theta(\boldsymbol{x}_t, t)$ as well as the mean $\boldsymbol{\mu}_\theta(\boldsymbol{x}_t, t)$ which can be predicted from $\boldsymbol{\epsilon}_\theta(\boldsymbol{x}_t, t)$. We use the models pretrained on AFHQ-Dog that is used in [9].

For the manipulation of 512×512 images from ImageNet dataset [49], we use the improved DDPM [36] pretrained model that is used in [16]. Different from 256×256 resolution models, self-attention blocks are added to the Res block at the resolution of $8 \times 8, 16 \times 16$ and 32×32 resolution.

D. Details and More Results of Comparison

D.1. Reconstruction

Here, we provide details on the quantitative comparison of reconstruction performance between our diffusion-based inversion and SOTA GAN inversion methods, which results are presented in Sec 4.1 and Tab. 1 of our main text.

Baseline models. We use optimization approach [1], pixel2style2pixel (pSp) encoder [45], Encoder for Editing (e4e) [55], ReStyle encoder [3] and HFGI encoder [58] as our baseline models. pSp encoder adopts a Feature Pyramid Network and [32] inverts the image into $\mathcal{W}+$ space of StyleGAN. In contrast, e4e converts the image to the latent in $\mathcal{W}$ space, which enables to explain the trade-offs between distortion and editing quality. Restyle encoder is a residual-based encoder, improving its performance using iterative refinement. HFGI encoder further improves the inversion performance leveraging the adaptive distortion alignment module and the distortion consultation module.

Comparison setting. We followed the experimental settings as described in [58]. We invert the first 1,500 CelebA-HQ images. Then, we measure the quality of reconstruction from the inverted latent using MAE, LPIPS, SSIM metrics. All results except the result of our method are from the [58]. For our method, we set $(S_{\text{for}}, S_{\text{gen}})$ to (200, 40), which is our general setting.

D.2. Human Evaluation

Comparison setting. We conduct user study to evaluate real face image manipulation performance on CelebA-HQ [27] with our method, StyleCLIP global direction (GD) [39] and StyleGAN-NADA [20]. We get 6,000 votes from

50 people using a survey platform. We use the first 20 images in CelebA-HQ testset as general cases and use another 20 images with novel views, hand pose, and fine details as hard cases. For a fair comparison, we use 4 in-domain attributes (angry, makeup, beard, tanned) and 2 out-of-domain attributes (zombie, sketch), which are used in the studies of baselines. Here, we use official pretrained checkpoints and implementation for each approach. We ask the respondents to rank the models by how well the image is manipulated, representing the property of the target attribute and preserving important semantics of the objects.

Results used for evaluation. We provide manipulation results by our method, StyleCLIP-GD and StyleGAN-NADA, which are used for human evaluation, in Fig. 25, 26.

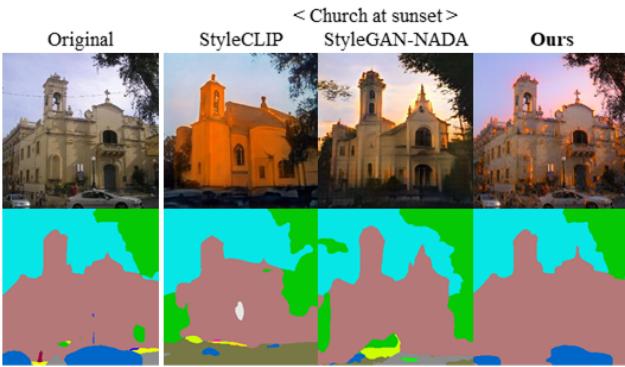### D.3. Quantitative Evaluation

Figure 16. Example of segmentation results from the manipulation results by different methods.

Quality metrics. We use the following quality metrics for quantitative evaluation: Directional CLIP similarity ($\mathcal{S}_{\text{dir}}$), segmentation-consistency (SC), and face identity similarity (ID). Specifically, $\mathcal{S}_{\text{dir}}$ is defined as follows:

$$\mathcal{S}_{\text{dir}}\left(\boldsymbol{x}_{\text{gen}}, y_{\text{tar}}; \boldsymbol{x}_{\text{ref}}, y_{\text{ref}}\right) := \frac{\langle \Delta I, \Delta T \rangle}{\|\Delta I\| \|\Delta T\|}, \qquad (30)$$

where

$$\Delta T = E_T(y_{\text{tar}}) - E_T(y_{\text{ref}}), \Delta I = E_I(\boldsymbol{x}_{\text{gen}}) - E_I(\boldsymbol{x}_{\text{ref}}).$$

Here, E_I and E_T are CLIP's image and text encoders, respectively, and y_{tar}, $\boldsymbol{x}_{\text{gen}}$ are the text description of a target and the generated image, respectively. Also, y_{ref}, $\boldsymbol{x}_{\text{ref}}$ denote the source domain text and image, respectively. Next, SC is a pixel accuracy when the segmentation result from $\boldsymbol{x}_{\text{ref}}$ by the pretrained segmentation model is set as the label and the result from $\boldsymbol{x}_{\text{gen}}$ is set as the prediction, as shown in Figure 16. Lastly, ID $:= L_{\text{face}}(\boldsymbol{x}_{\text{gen}}, \boldsymbol{x}_{\text{ref}})$ where $\mathcal{L}_{\text{face}}$ is the face identity loss in [15].

Our goal is to achieve the better score in terms of $\mathcal{S}_{\text{dir}}$, SC, and ID to demonstrate high attribute-correspondence ($\mathcal{S}_{\text{dir}}$) as well as well-preservation of identities without unintended changes (SC, ID).

Comparison setting. To compute $\mathcal{S}_{\text{dir}}$, we use a pretrained CLIP [41]. To calculate SC, we use pretrained face parsing network [63] and semantic segmentation networks [67, 68]. To compute ID, we use a pretrained face recognition [15] model. Then, we performed comparison with StyleCLIP [39] and StyleGAN-NADA [20]. We use 1,000 test images from CelebA-HQ [27] and LSUN-Church [64], respectively. We use the manipulation results for three attributes in CelebA-HQ (makeup, tanned, gray hair) and LSUN-Church (golden, red brick, sunset). These attributes are required to confirm that the manipulation results correspond to the target text without the changes of identities and shapes of the source objects.

D.4. Comparison of Church Image Manipulation

We additionally provide the manipulation of 256×256 church images from LSUN-Church [64] with StyleCLIP latent optimization (LO) [39] and StyleGAN-NADA [20] in Fig. 27.
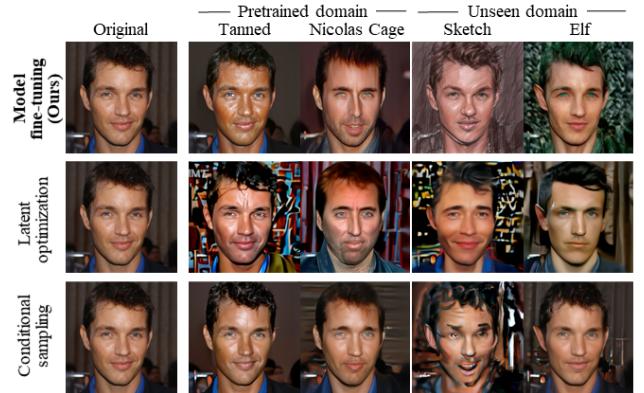
D.5. Diffusion-based Manipulations

Figure 17. Comparison between diffusion-based manipulation methods.

We compare our model fine-tuning method with latent optimization and conditional sampling method [16] guided by CLIP loss.

For the latent optimization of the diffusion models, we use the same objective (Eq. (10) in the main manuscript) as the model fine-tuning. However, we optimize the inverted latent $\hat{\boldsymbol{x}}_{t_0}$ instead of the model $\boldsymbol{\epsilon}_{\hat{\theta}}$. For conditional sampling, the sampling process is guided by the gradient of CLIP loss with respect to the latent as a classifier guides the process in [16]. This method requires a noisy classifier that can classify the image with noise, but the noisy CLIP model is

not publicly available and its training will be too expensive. To mitigate this issue, we use the method proposed by [35]. Instead of using noisy CLIP, they use the gradient from the normal CLIP loss with the predicted x_0 given x_t, which we denoted as $f_\theta(x_t, t)$ in Eq. (24) at every step.

In Fig. 17, we display a series of the real image manipulation given the text prompt by our model fine-tuning method, latent optimization and conditional sampling. We can see that the manipulation results via latent optimization and conditional sampling methods failed to manipulate the images to the unseen domain. The reason is that the manipulation using latent optimization and conditional sampling is restricted by the learned distribution of the pretrained model. On the other hand, the proposed model fine-tuning method shows superior manipulation performance.
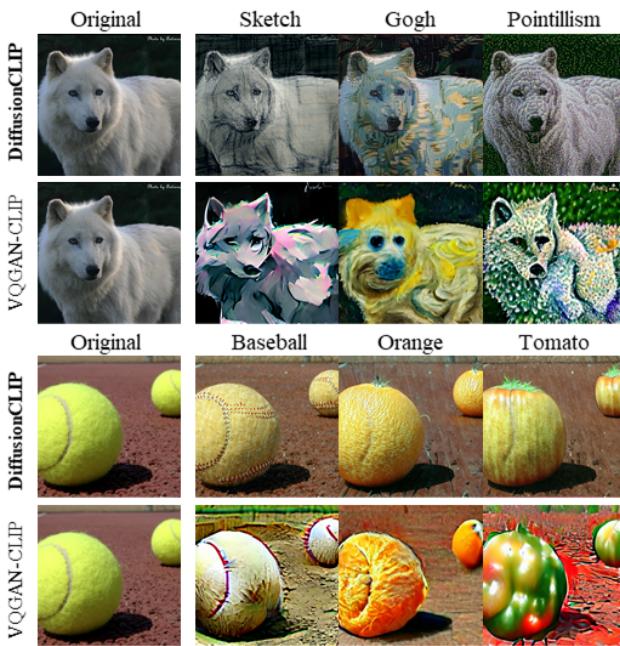
D.6. Other GAN Baselines

Figure 18. Comparison with VQGAN-CLIP [19,41] using 512×512 images from ImageNet [49]

Comparison with VQGAN-CLIP. VQGAN-CLIP [19, 41] recently show the impressive results of CLIP-guided conditional generation of artistic images. It also provides the style transfer, which optimizes the latent from the input image guided by CLIP loss. We compare DiffusionCLIP with VQGAN-CLIP for the manipulation of 512×512 images from ImageNet [49]. We follow official implementation for VQGAN-CLIP. For our method, we utilize GPU-efficient fine-tuning method with the diffusion model pretrained on 512×512 ImageNet which is used in [16]. We set $(S_{\text{for}}, S_{\text{gen}}) = (40, 12)$. In the first two rows of Fig. 18, our method successfully translates the image into target style,

preserving the identity of the object. However, the manipulation results by VQGAN-CLIP do not show representative properties of target styles. In the bottom two rows of Fig. 18, our method shows excellent semantic manipulation results preserving the details of backgrounds, while the results from VQGAN-CLIP show severe unintended changes.

Figure 19. Comparision with other GAN inversion-based manipulation: StyleSpace [61] and InterfaceGAN [50].

Other GAN inversion-based manipulation. We also compare our method with non text-driven manipulation methods based on GAN inversion: StyleSpace [61] and InterfaceGAN [50]. StyleSpace manipulates the latent inverted by e4e [55] in StyleGAN2 [29] $\mathcal{W}+$ space. InterfaceGAN manipulates the latent inverted by IDInvert [69] in StyleGAN [28] $\mathcal{W}+$ space. As shown in Fig. 19, StyleSpace and InterfaceGAN fail to manipulate the images with hand poses, suggesting practical limitations. However, our method successfully manipulates the images without artifacts.

E. Additional Results

Manipulation of 512×512 images from ImageNet. Here, we provide the results of the manipulation of 512×512 images from ImageNet [49]. We leverage GPU-efficient fine-tuning with the diffusion model pretrained on 512×512 ImageNet which is used in [16]. We set $(S_{\text{for}}, S_{\text{gen}}) = (40, 12)$. We set $(S_{\text{for}}, S_{\text{gen}}) = (40, 12)$ and other hyperparameters are equally applied as manipulation of 256×256 images. We first show the style transfer results of general images in Fig. 28. We show text-driven semantic manipulation results from tennis ball into other objects in Fig. 29. Finally, we show the manipulation of frog images in Fig. 30.

Image translation between unseen domains. In Fig. 31 we display additional results of image translation between unseen domains, where animation images, portrait art, and strokes are translated into Pixar, paintings by Gogh and Neanderthal men. Note that we do not require any curated dataset for both source and target domain.

Figure 20. Failure cases.

Failure cases. Due to the dependency on the performance of CLIP encoder, DiffusionCLIP sometimes fails to manipulate images as shown in Fig. 20. For example, it is difficult to manipulate human face images into objects such as computers, chairs, pencils. Also, manipulation to target controls that happen or become famous recently may fail because their representations are not reflected inside CLIP encoders.

F. Hyperparameter and Ablation Study

F.1. Dependency on S_{for}, S_{gen} and t_0

In Table 4, the reconstruction from the latents through the inversion process on face images are evaluated using MAE, LPIPS and SSIM. As S_{for} and S_{gen} increase, the reconstruction quality increases. However, in case that $S_{for} < S_{gen}$, the quality stays in the similar degree or even decreases, causing the artifacts as the cases of $(S_{for}, S_{gen}) = (6, 40)$ and $(S_{for}, S_{gen}) = (200, 6)$ in Fig. 10 in the main manuscript. When (S_{for}, S_{gen}) is fixed, as the return step t_0 increases, the quality decreased because the intervals between the steps become larger.

F.2. Identity Loss

Figure 21. Ablation study of identity loss.

Here, we analyze the importance of identity loss. We use ℓ_1 loss as the identity loss, and in the case of human face image manipulation, the face identity loss in [15] is used. Whether to use these identity losses is determined by the target control. We show the examples in Fig. 21. If preserving the identity of the human face is important for the target control such as 'Makeup', it is recommended to use face identity loss as we can see in the first row in Fig. 21. ℓ_1 can help further preserve the background details. If the target control doesn't require the exact identity preserving

as artistic transfer as the second rows of Fig. 21, the identity loss can hinder the change. The examples of usage of hyperparameters depending on the target text prompts are represented in Table 5.
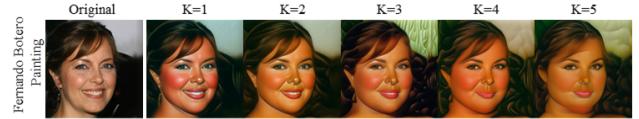
F.3. Dependency on Fine-tuning Epochs K

Figure 22. Changes according to the fine-tuning epochs.

To fine-tune diffusion models, we use Adam optimizer with an initial learning rate of 4e-6 which is increased linearly by 1.2 per 50 iterations. Hence, as we can see in the example of changes are represented in Fig. 22, the images generated from the fine-tuned models change closer to the target control as the epoch K increases.

F.4. Dependency on the Number of Precomputed Images N
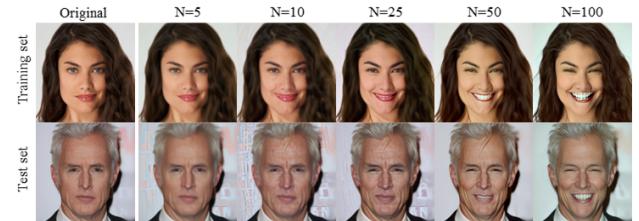

Figure 23. Dependency on the number of precomputed images N

As we mentioned before, if several latents have been precomputed, we can further reduce the time for fine-tuning by recycling the latent to synthesize other attributes. In this case, the number of precomputed images N is a hyperparameter to be controlled. We test the cases with different N. We fine-tune the models with $N = 5, 10, 25, 50, 100$, fixing the learning rates to 4e-6 and the number of iterations to 100. We found that as increasing the N, the image can be manipulated more as shown as Fig. 23.
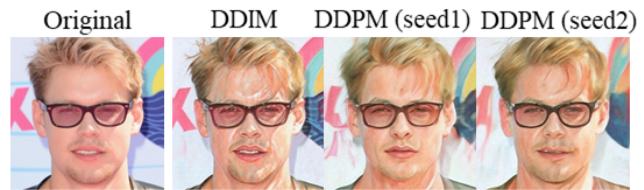
F.5. Stochastic Manipulation

Figure 24. Effect of stochastic manipulation with random seeds.

Table 4. Quantitative analysis on reconstruction quality with respect to S_{for}, S_{gen} and t_0.

t_0	S_{for}	S_{gen}	MAE ↓	LPIPS ↓	SSIM ↑	t_0	S_{for}	S_{gen}	MAE ↓	LPIPS ↓	SSIM ↑
		6	0.047	0.185	0.732			6	0.065	0.237	0.602
	6	40	0.061	0.221	0.704		6	40	0.085	0.286	0.615
		200	0.063	0.224	0.694			200	0.090	0.292	0.602
		6	0.027	0.110	0.863			6	0.037	0.148	0.779
300	40	40	0.023	0.091	0.891	500	40	40	0.027	0.109	0.868
		200	0.023	0.086	0.895			200	0.026	0.101	0.874
		6	0.024	0.095	0.885			6	0.032	0.126	0.827
	200	40	0.020	0.073	0.914		200	40	0.022	0.082	0.901
		200	0.019	0.065	0.923			200	0.021	0.073	0.912
		6	0.055	0.208	0.673			6	0.084	0.283	0.501
	6	40	0.073	0.255	0.655		6	40	0.101	0.325	0.564
		200	0.077	0.260	0.643			200	0.106	0.330	0.552
		6	0.031	0.128	0.827			6	0.047	0.175	0.706
400	40	40	0.025	0.100	0.880	600	40	40	0.029	0.120	0.852
		200	0.024	0.093	0.885			200	0.028	0.108	0.862
		6	0.028	0.108	0.862			6	0.041	0.147	0.778
	200	40	0.024	0.076	0.910		200	40	0.024	0.087	0.893
		200	0.020	0.068	0.919			200	0.022	0.076	0.907

We analyzed how the results change when stochastic DDPM sampling is used rather than deterministic DDIM sampling. As shown in Figure 24, the images can be modified in many ways, which can be useful for artistic transfer.

F.6. Hyperparameters according to Target Text y_{tar}

We provide examples of hyperparameter settings according to y_{tar} in Table 5. Our method has a similar number of hyperparameters as other text-driven methods such as StyleCLIP [39] and StyleGAN-NADA [20]. In our method, the actual hyperparameters for different controls are just t_0, λ_{L1}, λ_{ID}. These can be chosen simply based on insight as to whether the target requires severe shape changes. The target controls demanding severe changes of shape or color such as change of species or artistic style transfer require high t_0 without no identity losses, while the target controls were preserving the identity of the object is important to require low t_0 and the use of identity losses.

G. Running Time and Resources

Here, we provide the details on the running time of training and inference for each procedure using NVIDIA Quadro RTX 6000 in the case of manipulating 256×256 size images.

DiffuisonCLIP fine-tuning. As illustrated in Sec B.1, DiffusionCLIP fine-tuning process can be split into the latent precomputing procedure and the model updating procedure. The latent precomputing procedure is carried out just once for the same pre-trained diffusion. When we use S_{for} of 40 as normal, the inversion for each image takes 1.644 seconds (all the reported times are the average times of 30 iterations). So, when we precompute the latents from the 50 images,

it finished at about 82.2 seconds. For the model updating process, one update step including the generative process, loss calculation, and taking a gradient step takes 0.826 seconds when the batch size is 1 and S_{gen} is 6. So, 1 epoch with 50 precomputed image-latent pairs takes 41.3 seconds. The total epochs K are range from 1 to 10 depending on types of the target text y_{tar}, so the total time for the model updating takes from 41.3 seconds to 7 minutes.

When using GPU-efficient model updating, loss calculation and taking a gradient step takes 1.662 seconds which is almost twice as the original fine-tuning. Therefore, total fine-tuning time will be increased as twice.

The latent precomputing procedure requires about 6GB. The original model and GPU-efficient model updating require 23GB and 12GB of VRAM, respectively.

Manipulation of images from pretrained domain. With the quick manipulation $(S_{\text{for}}, S_{\text{gen}}) = (40, 6)$, it takes 1.644 seconds and 0.314 seconds for the inversion process and the generative process, respectively, resulting in 1.958 seconds total. The quick manipulation still produces great results that can be well used for image manipulation in practice. When we set $(S_{\text{for}}, S_{\text{gen}})$ to $(200, 40)$, it takes 8.448 seconds and 1.684 seconds for the inversion process and the generative process respectively, leading to 10.132 seconds in total. This application and the following applications all require at least 6GB of VRAM.

Image translation between unseen domains. Image translation between unseen domains and stroke-conditioned unseen domain generation requires K_{DDPM} forward DDPM and reverse DDIM process added to one forward and reverse

Table 5. Examples of hyperparameter settings according to y_{tar}.

Type	y_{tar}	y_{ref}	t_0	λ_{L1}	λ_{ID}
Human face	Tanned face	face	300	0.3	0.3
	Face with makeup	Face	300	0.3	0.3
	Face without makeup	Face	300	0.3	0.3
	Angry face	face	500	0.3	0.3
	Person with beards	Person	400	0.3	0.3
	Person with curly hair	Person	400	0.3	0.3
	Person with red hair	Person	500	0.3	0.3
	Person with grey hair	Person	500	0.3	0.3
	Old person	person	400	0.3	0.3
	Mark Zuckerberg	Person	600	0.3	0
	Painting by Gogh	photo	600	0	0
	Painting in Modigliani style	Photo	600	0	0
	Sketch	Photo	600	0.3	0
	3D render in the style of Pixar	Photo	600	0.3	0
	Portrait by Firda Kahlo	Photo	600	0.3	0
	Super Saiyan	Human	600	0	0
	Tolken elf	Human	600	0	0
	Zombie	Human	600	0	0
	The Jocker	Human	600	0	0
	Neanderthal	Human	600	0	0
Dog face	Smiling Dog	Dog	600	0.3	-
	Yorkshire Terrier	Dog	600	0	-
	Hamster	Dog	600	0	-
	Bear	Dog	500	0	-
	Wolf	Dog	500	0	-
	Fox	Dog	500	0	-
	Nicolas Cage	Dog	600	0	-
	Zombie	Dog	600	0.3	-
	Venom	Dog	600	0.3	-
	Painting by Gogh	Photo	500	0.3	-
Church	Red brick wall church	church	300	0.3	-
	Golden church	church	400	0.3	-
	Snow covered church	church	500	0.3	-
	Wooden house	church	500	0.3	-
	Ancient traditional Asian tower	church	500	0.3	-
	Departmetn store	church	500	0.3	-
Bedroom	Blue tone bedroom	bedroom	500	0.3	-
	Green tone bedroom	bedroom	500	0.3	-
	Wooden bedroom	bedroom	500	0.3	-
	Golden bedroom	bedroom	400	0.3	-
	Palace bedroom	bedroom	500	0.3	-
	Princess bedroom	bedroom	500	0.3	-
	Watercolor art with thick brushstrokes	Photo	600	0.3	-

DDIM process. Thanks to the possibility of the sampling x'_t in closed form, the time for forward DDPM and reverse DDIM process can be reduced into the time for the reverse DDIM process 0.314 seconds when $S_{\text{gen}} = 6$. K_{forward} is set to 1-10, so K_{DDPM} forward DDPM and reverse DDIM process takes 0.314-3.14 seconds. When time for one forward and reverse DDIM process is added, the whole process takes 2.272-5.098 seconds with $(S_{\text{for}}, S_{\text{gen}}) = (40, 6)$ and 10.446-13.272 seconds with $(S_{\text{for}}, S_{\text{gen}}) = (200, 40)$.

Multi-attribute transfer. We can change multiple attributes through only one generative process. It takes 2.602 seconds when $(S_{\text{for}}, S_{\text{gen}}) = (40, 6)$ and 14.744 seconds when $(S_{\text{for}}, S_{\text{gen}} = (200, 40)$.

Trade-off between the inference time and preparation time. Latent optimization-based manipulation methods [39] do not require the preparation time for the manipu-

lation. However, they require an optimization process per image. In contrast, our fine-tuning methods, latent mapper in StyleCLIP [39] and StyleGAN-NADA [20] require the set-up for manipulation, which is training the model. However, once the model is fine-tuned, we can apply the model to all images from the same pretrained domain. In terms of training time, our method takes 1-7 minutes, which is faster than the latent mapper of StyleCLIP (10-12hours) and similar to StyleGAN-NADA (a few minutes).

Increasing image size. We found that as the image size is increased from 256×256 to 512×512, the running time for each procedure increased as 4 times, and GPU usage increased as twice.

H. Societal Impacts

DiffusionCLIP enables high-quality manipulation of images for people using simple text prompts without professional artistic skills. However, this manipulation can be used maliciously to confuse people with realistic manipulated results. Therefore, we advise users to make use of our method properly. We also advise you to make use of our method carefully for proper purposes.

In this work, we use two types of pretrained models, CLIP [41] and the diffusion models, to manipulate images without additional manual efforts for new target controls. Image encoder and text encoder of CLIP are trained on 400 million image-text pairs gathered from publicly available sources on the internet to learn visual concepts from natural language supervision. However, although the size of the training dataset is huge, it is not enough for the models to learn general balanced knowledge. As the authors in [41] acknowledged the potential issues from model biases, manipulation using CLIP can introduce biased results. Diffusion models trained on CelebA-HQ [27], AFHQ-dog [12], LSUN-Bedroom, LSUN-Church [64] and ImageNet [49] used in our models can generate biased results during iterations. Especially, the generative models trained on the CelebA-HQ dataset that is composed of face images of celebrities are founded to produce face images of attractive people who are mostly 20-40 years old [18]. We hope that more research is conducted in direction of generative models and representation learning that resolve the bias issues.
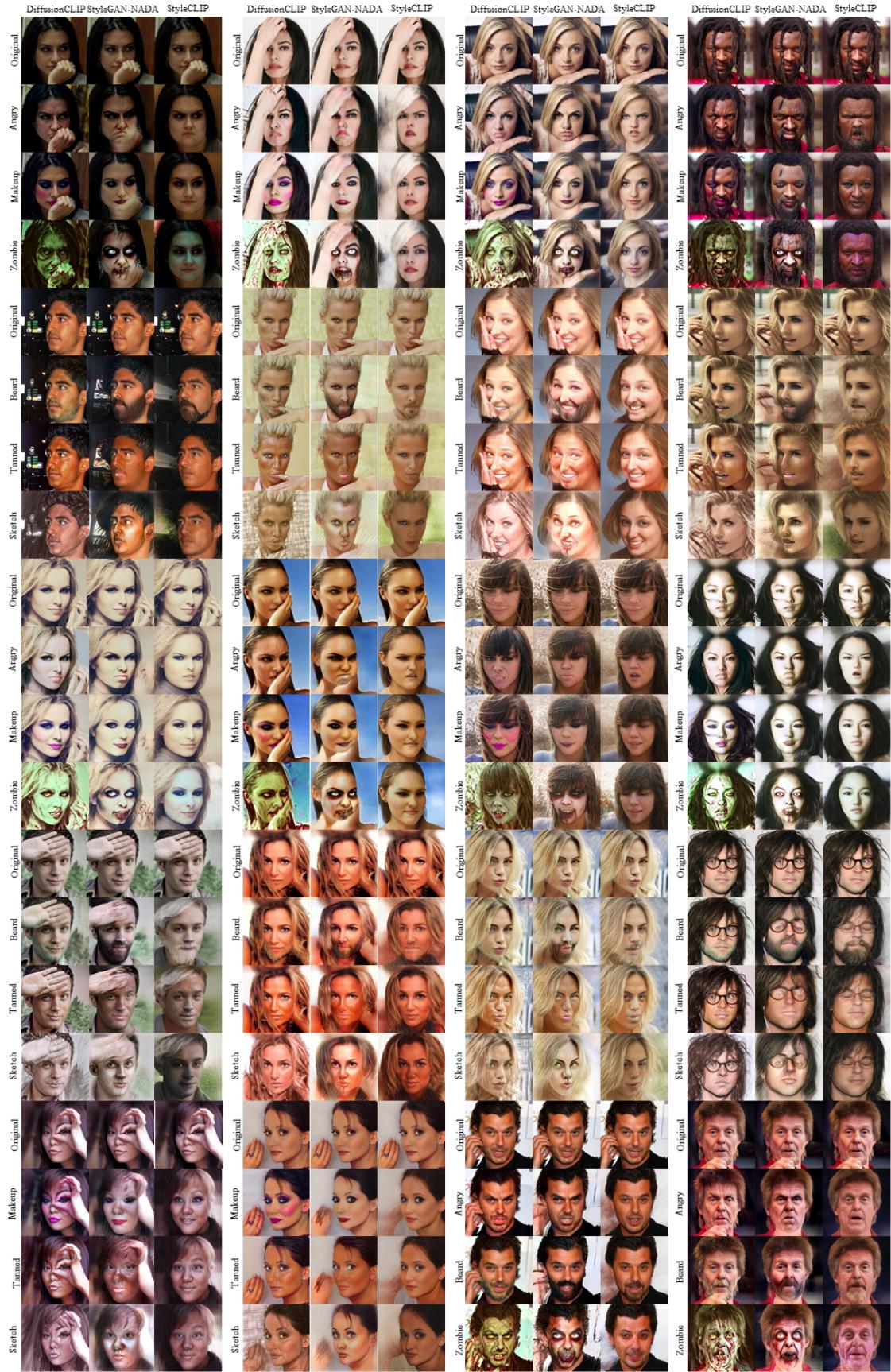
Figure 25. Manipulation of hard cases that are used for human evaluation. Hard cases include 20 images with novel poses, views and details in CelebA-HQ [27]. We compare our method with StyleCLIP global direction method [39] and StyleGAN-NADA [20].

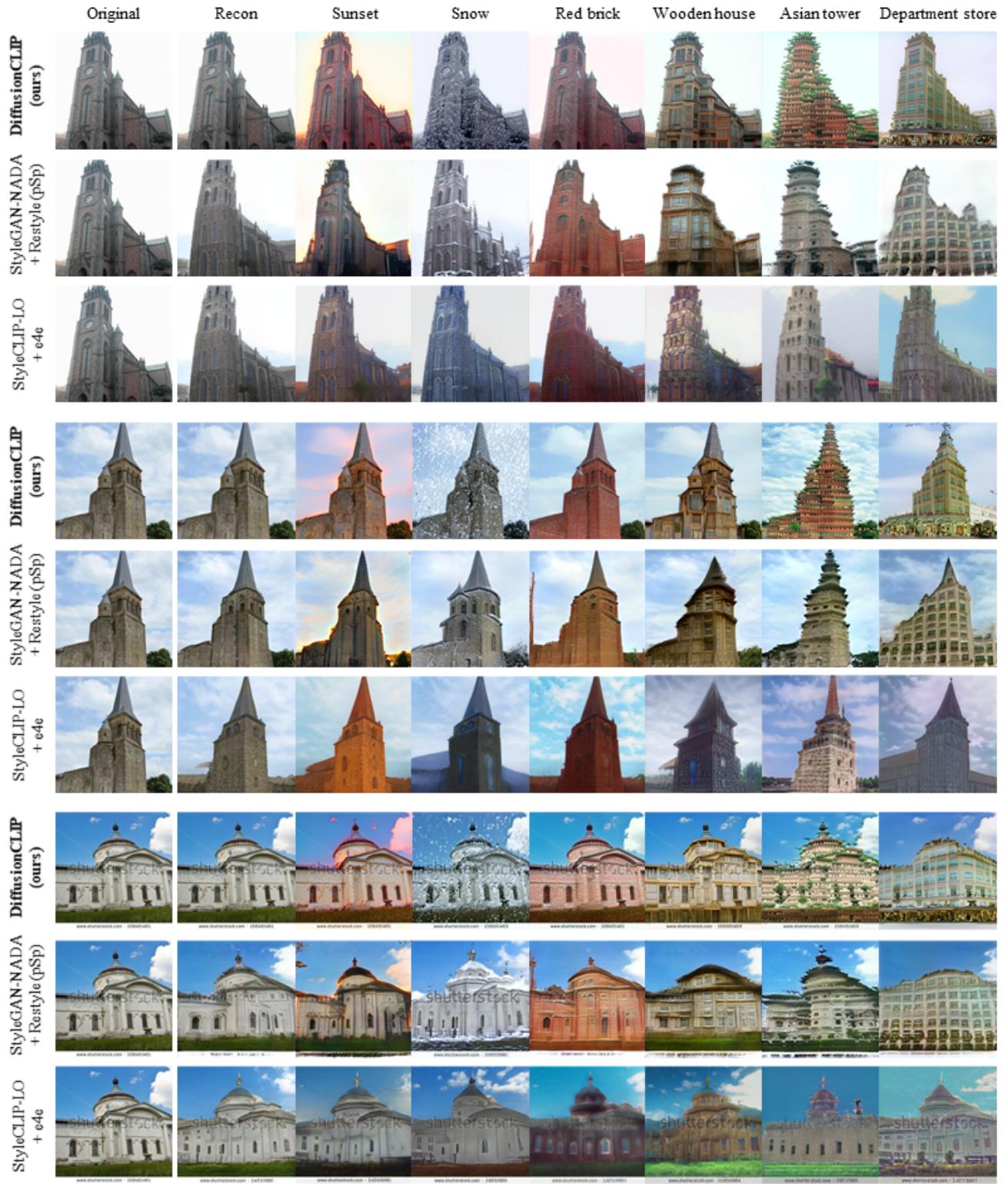Figure 26. Manipulation of general cases that are used for human evaluation. General cases include the first 20 images in CelebA-HQ testset [27]. We compare our method with StyleCLIP global direction method [39] and StyleGAN-NADA [20].

Figure 27. Qualitative comparison of church image manipulation performance with StyleCLIP global direction method [39] and StyleGAN-NADA [20].

Figure 28. Manipulation of 512×512 images using the ImageNet [49] pretrained diffusion models.
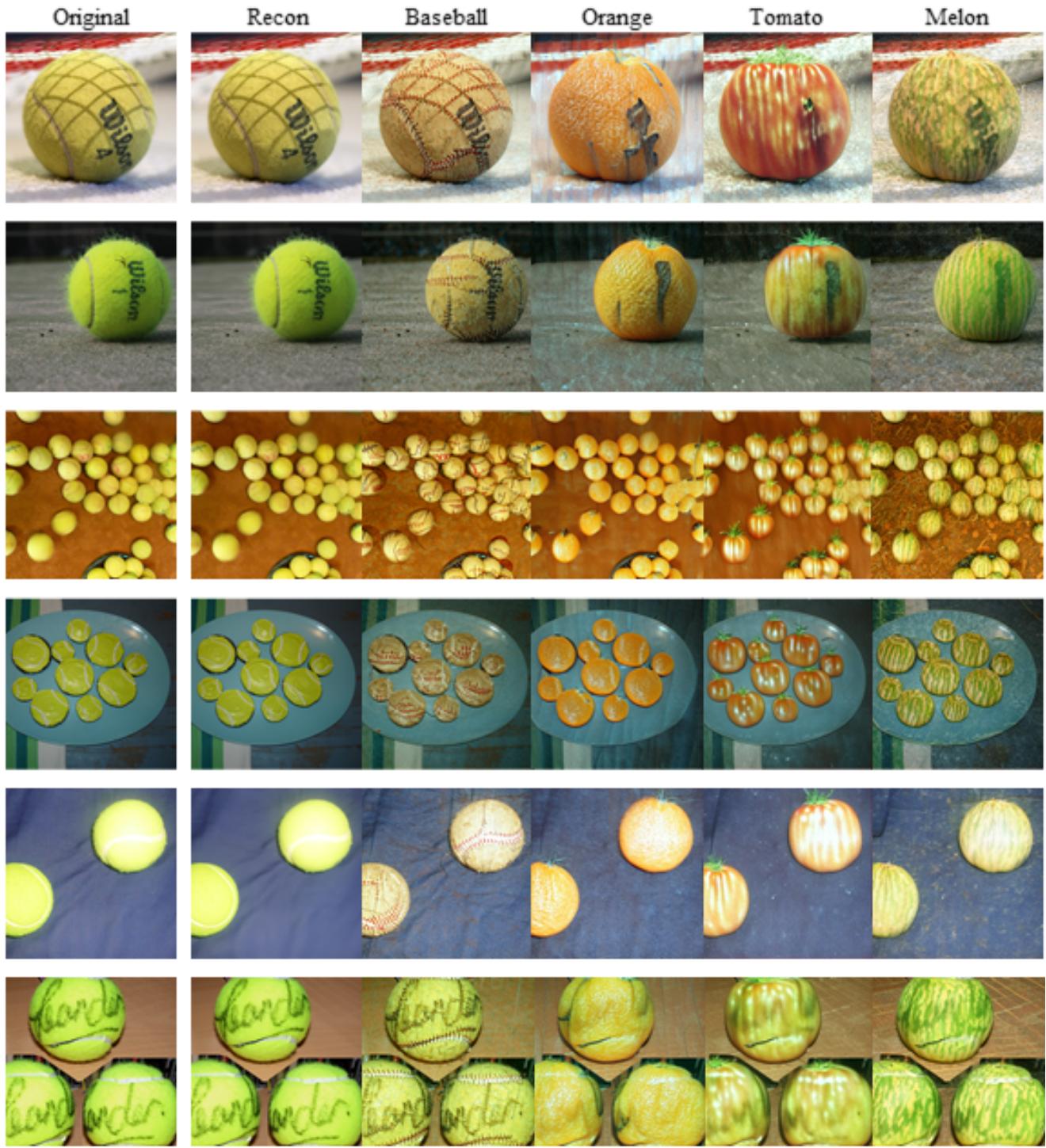
Figure 29. Manipulation of 512×512 images of tennis balls using the ImageNet [49] pretrained diffusion models.
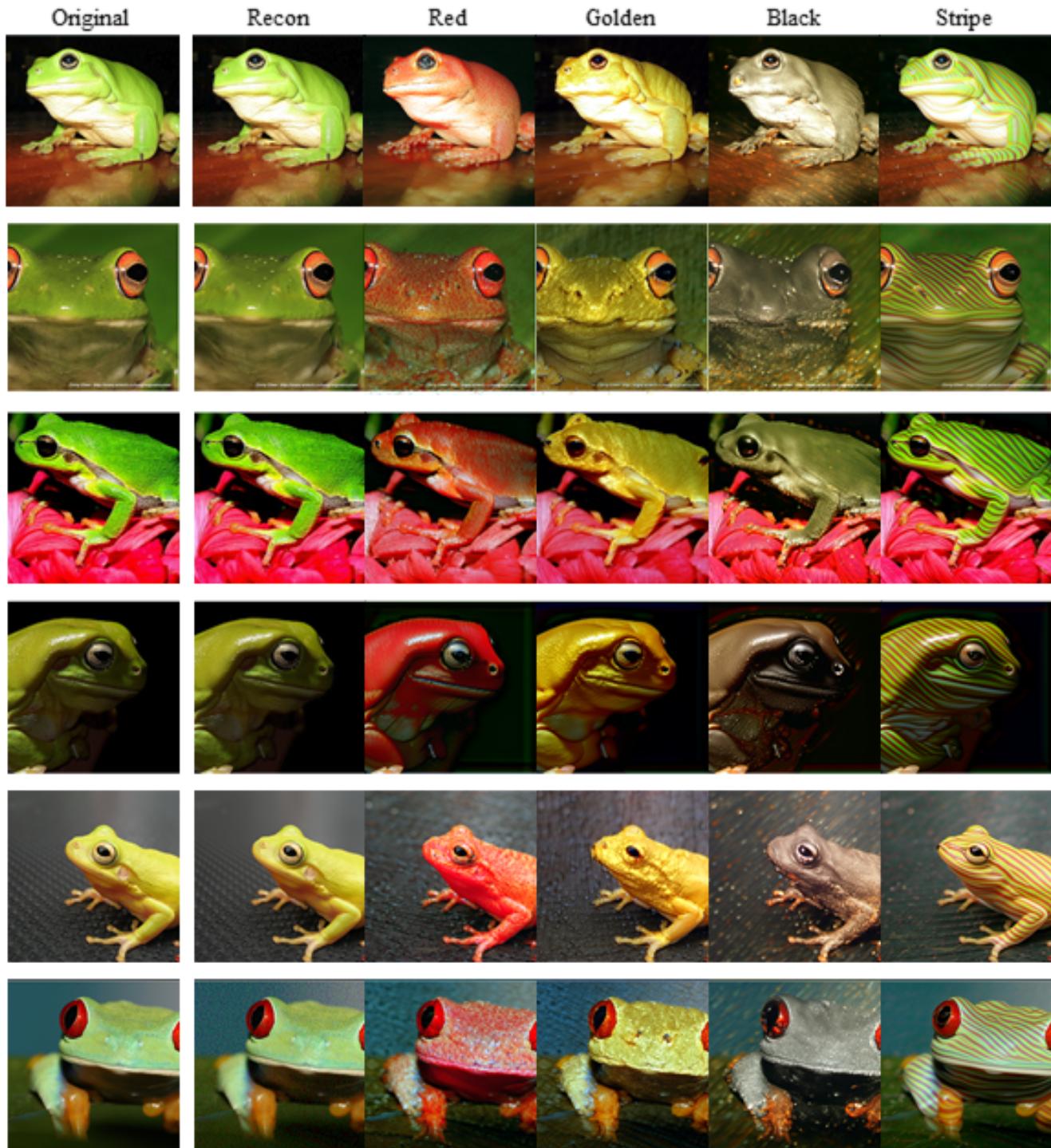
Figure 30. Manipulation of 512×512 images of frogs using the ImageNet [49] pretrained diffusion models.

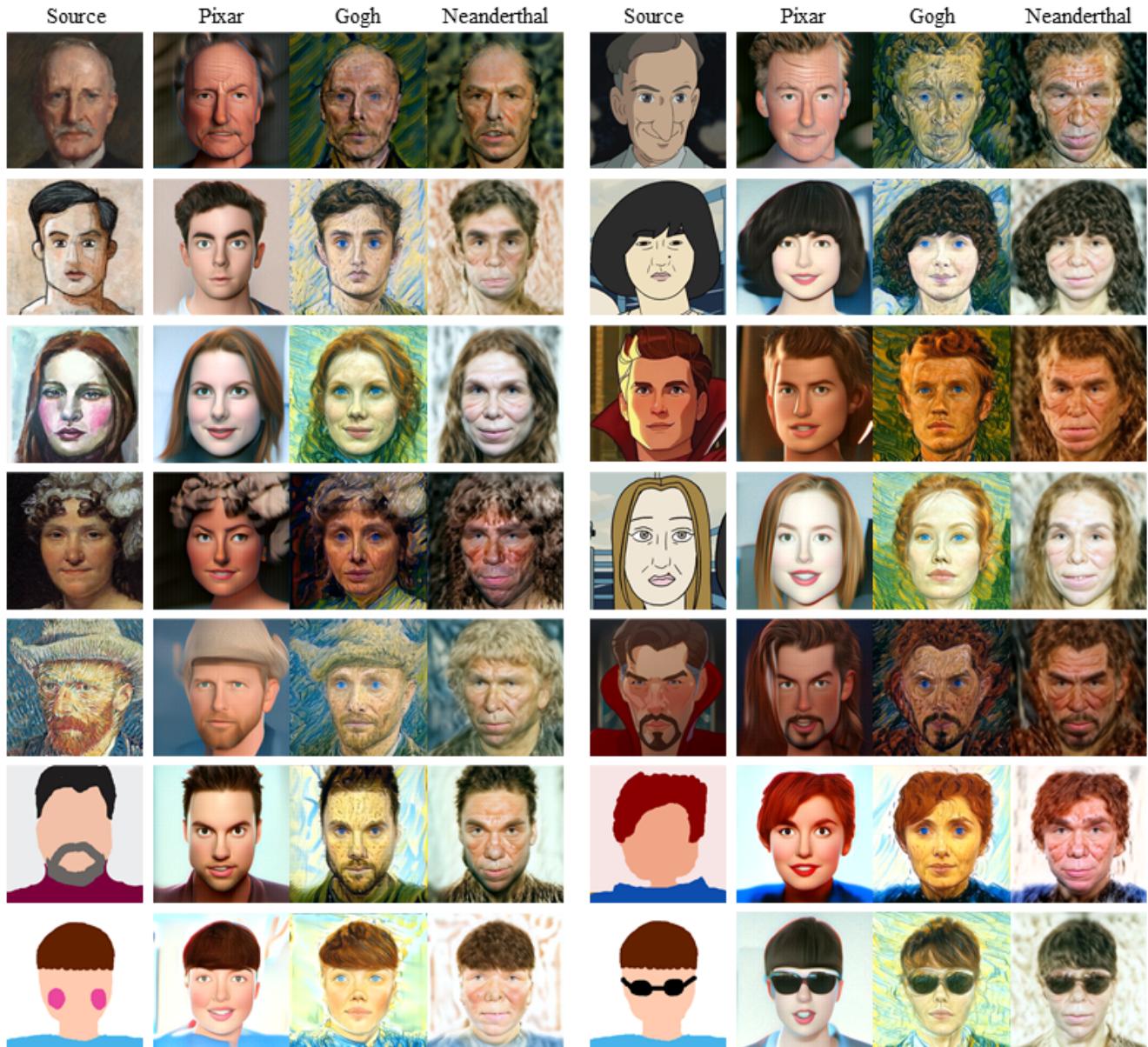| Source | Pixar | Gogh | Neanderthal | Source | Pixar | Gogh | Neanderthal |

Figure 31. Additional results of image translation between unseen domains.